

UCLA

UCLA Electronic Theses and Dissertations

Title

Spin-Orbit Torques in Topological Insulators

Permalink

<https://escholarship.org/uc/item/3ds9792s>

Author

Shao, Qiming

Publication Date

2015

Peer reviewed|Thesis/dissertation

UNIVERSITY OF CALIFORNIA
Los Angeles

Spin-Orbit Torques in Topological Insulators

A thesis submitted in partial satisfaction
of the requirements for the degree Master of Science
in Electrical Engineering

by

Qiming Shao

2015

ABSTRACT OF THE THESIS

Spin-Orbit Torques in Topological Insulators

by

Qiming Shao

Master of Science in Electrical Engineering

University of California, Los Angeles, 2015

Professor Kang Lung Wang, Chair

Spin torque can toggle magnetization state of nanomagnets in magnetic tunnel junctions. In heavy metals, giant Spin Hall Effect gives rise to a large spin-orbit torque (SOT) enabling magnetization switching of adjacent ferromagnets. Spin torque ratio is the key parameter in determining energy efficiency. Recently, a giant SOT was demonstrated in topological insulators (TIs), which are a class of materials owing insulating bulk and metallic surface states. Although several theoretical studies show that spin-momentum locking of surface states generates this giant SOT, experimental clarification is still lacking. In this thesis, we use the second-harmonic anomalous Hall resistance to access the current-induced spin-orbit fields (and thus SOTs). Heavy metal/ferromagnet heterostructure, Ta/CoFeB/MgO, is used to verify the validation of this method. Then, we quantitatively estimate the SOT in different TI/chromium-doped TI heterostructures with

different magnetic dopant positions, which shows the evidence of surface states originated SOTs. At last, we show that the magnitude of SOTs can be controlled by the gate voltage due to its semiconducting nature. All these studies may contribute to the future low power spintronics.

The thesis of Qiming Shao is approved.

Yaroslav Tserkovnyak

Chandra J. Joshi

Kang Lung Wang, Committee Chair

University of California, Los Angeles

2015

Dedicated to my beloved Yuan

Table of Contents

Chapter 1. Introduction – spin-torque building blocks in modern technology	1
1.1 Spintronics before spin torque	1
1.1.1 Advantage of spintronics: no standby power	1
1.1.2 GMR and TMR	1
1.1.3 Magnetic field required to write.....	3
1.2 Spin-transfer torque and voltage-controlled magnetic anisotropy.....	5
1.2.1 Spin-transfer torque	5
1.2.2 Voltage-controlled magnetic anisotropy.....	9
1.3 Spin-orbit torque.....	12
1.3.1 General expression for spin-orbit torque and Hall resistance	12
1.3.2 Rashba effect and Spin Hall Effect.....	15
1.3.3 Spin-orbit torque MRAM.....	20
1.4 Thesis outline	22
Chapter 2. Spin-orbit torque in heavy metals and topological insulators.....	24
2.1 Heavy metal/ferromagnet heterostructure for SOT study	24
2.1.1 Harmonic analysis for SOT study	24
2.1.2 Current-induced magnetization switching	31
2.2 SOT in TI/Cr-TI bilayer and Cr-TI single layer	34
2.2.1 Motivation for studying SOT in TIs	34
2.2.2 Experimental demonstration of giant SOTs in Cr-TI/TI bilayer	37
2.2.3 SOTs in uniform Cr-TI single layer	42
2.3 Current-induced magnetization switching in magnetic TIs	45
Chapter 3. Evidences for surface state spin-orbit torque in TIs	47
3.1 Model for surface state induced SOTs.....	47
3.2 Magnetic doping position dependent study	54
3.3 Electric-field controlled SOT	58
Chapter 4. Summary and outlook.....	63
References	64

Acknowledgments

First and foremost, I would like to express my sincere gratitude to my advisor, Professor Kang L. Wang, for his supervision and support. I also would like to thank Dr. Yabin Fan for guiding me to do the transport measurement and sharing data with me. Note that the data for topological insulator related study in this thesis are mostly not published yet: some are in a paper under review and others are in a manuscript in preparation.

Chapter 1. Introduction – spin-torque building blocks in modern technology

1.1 Spintronics before spin torque

1.1.1 Advantage of spintronics: no standby power

Modern electronics have approaching their scaling limit due to scaling of MOSFET. Leakage power, i.e. standby power, has increased dramatically as the technology node gets smaller and smaller. (Technology node is the half pitch between two adjacent DRAM metal lines, or the minimum feature size that can be “printed” by the lithography technique.) As the name of leakage power indicates, the electronics consume power due to leakage current, since power supply is required to be on even when they do not operate. In traditional CMOS technology, memory parts include SRAM, DRAM and Flash. SRAM has a very fast speed (~ 0.2 ns) [1], but it requires continuous voltage supply to maintain the stored value. As the channel length shortens, the direct tunneling and other short channel effect make the MOSFETs in SRAM leaky. For DRAM, it has a relatively longer read/write time (< 10 ns for stand-alone applications and 1-2 ns for embedded applications), and it also needs refreshment every 64 ms, which consumes the most energy. [1] For Flash memory, it is nonvolatile, but it requires high voltage to write (> 8 V), that makes it not compatible with on-chip applications. [1] So, people are thinking of alternative solutions to electronics.

1.1.2 GMR and TMR

Spintronics is the one of choices thanks to its nonvolatile nature. Since the discovery of giant magnetoresistance (GMR) [2, 3], magnetic multilayer stacks (later on called spin valves) have progressively led spintronics to our real life. Later even larger tunneling magnetoresistance (TMR)

is observed in magnetic tunnel junctions (MTJs). Magnetoresistance is an effect of materials that changes resistance when a magnetic field is applied. Two important reasons for this phenomenon is geometric magnetoresistance (direct effect) and magnetization change due to magnetic field (indirect effect). For the geometric magnetoresistance, the resistance change is due to Lorentz force that carriers are felt in the magnetic field (see Eq. 1).

$$\mathbf{v} = \mu(\mathbf{E} + \mathbf{v} \times \mathbf{B}) \quad (1)$$

By solving the velocity, we obtain the Eq. 2 for the dependence of velocity on the electric field and magnetic field. Furthermore, we can obtain the relation between resistivity and external magnetic field (see Eq. 3).

$$\mathbf{v} = \frac{\mu}{1 + (\mu B)^2} (\mathbf{E} + \mu \mathbf{E} \times \mathbf{B} + \mu^2 (\mathbf{B} \cdot \mathbf{E}) \mathbf{B}) \quad (2)$$

$$\rho = \frac{1 + (\mu B)^2}{qn\mu} = \frac{1 + (\mu B)^2}{\sigma_0} = (1 + \mu^2 B^2) \rho_0 \quad (3)$$

So, for a typical semiconductor or metal, the increase of resistance in the presence of magnetic field is proportional the square of magnitude of magnetic field, which is typically observed as parabolic magnetoresistance background in semiconductors or metals.

For magnetoresistance due to magnetic field induced magnetization change, it has a fundamental mechanism: the current encounters more spin-dependent scattering in antiparallel state than in parallel state. It can be either in-plane current or perpendicular current relative to the magnetization plane. For a MTJ, it consists of two ferromagnetic layers sandwiched by a nonmagnetic tunnel barrier. The TMR ratio between parallel state and antiparallel state is a very important factor in determining MTJs' performance as a memory, in particular read speed and variability (the ability against random distribution of array parameters, such as MTJ pillar diameter and ferromagnetic layer thickness). In the following content, we indistinguishably use TMR (MR) for TMR (MR) itself and TMR (MR) ratio, but their meaning should be clear depending on the context.

1.1.3 Magnetic field required to write

We have MTJs that store the information without standby power, and we can read them anytime we want without worry about losing information. Typically, the memory made by MTJs is called magnetic random access memory (MRAM). In addition, we define the antiparallel state (high resistance) as “1”, and parallel state (low resistance) as “0”.

Now, it's time to consider the write, i.e. how to input the information to MTJs. We need a magnetic field to control the relative magnetization state between two ferromagnetic layer, either parallel or antiparallel. In the initial report done by M. N. Baibich *et al.* [3], Fe(001)/Cr(001) superlattice (see Figure 1-1d) was utilized to achieve a very high MR (GMR). Iron (Fe) is a ferromagnet, and it has spontaneous (net) magnetization in the absence of magnetic field below its Curie temperature (that depends on the material detail, and is different for bulk and thin film). Figure 1-1a gives a typical magnetic hysteresis along the easy axis x direction. Chromium (Cr) is an antiferromagnet and could pin the magnetization state of an adjacent ferromagnetic layer through the exchange bias. With the exchange coupling between antiferromagnet and ferromagnet, ferromagnetic hysteresis could have either negative or positive bias (see Figure 1-1b-c), and if exchange coupling is strong enough, it could pin the magnetization state of the ferromagnet along a specific direction (against a certain magnitude of field depending on the strength of exchange bias). M. N. Baibich *et al.* [3] observed a relatively small resistance when a large field was applied compared with zero field resistance (see Figure 1-1e). This phenomenon was explained well in terms of spin-dependent scattering. A large external magnetic field pushes the MTJ into the parallel state and thus a lower resistance. (Since the easy axes of Fe layer are along $\pm x$ direction, required external field along in-plane direction to push the MTJ into the parallel state is smaller than that along out-of-plane direction, as shown in Figure 1-1e.)

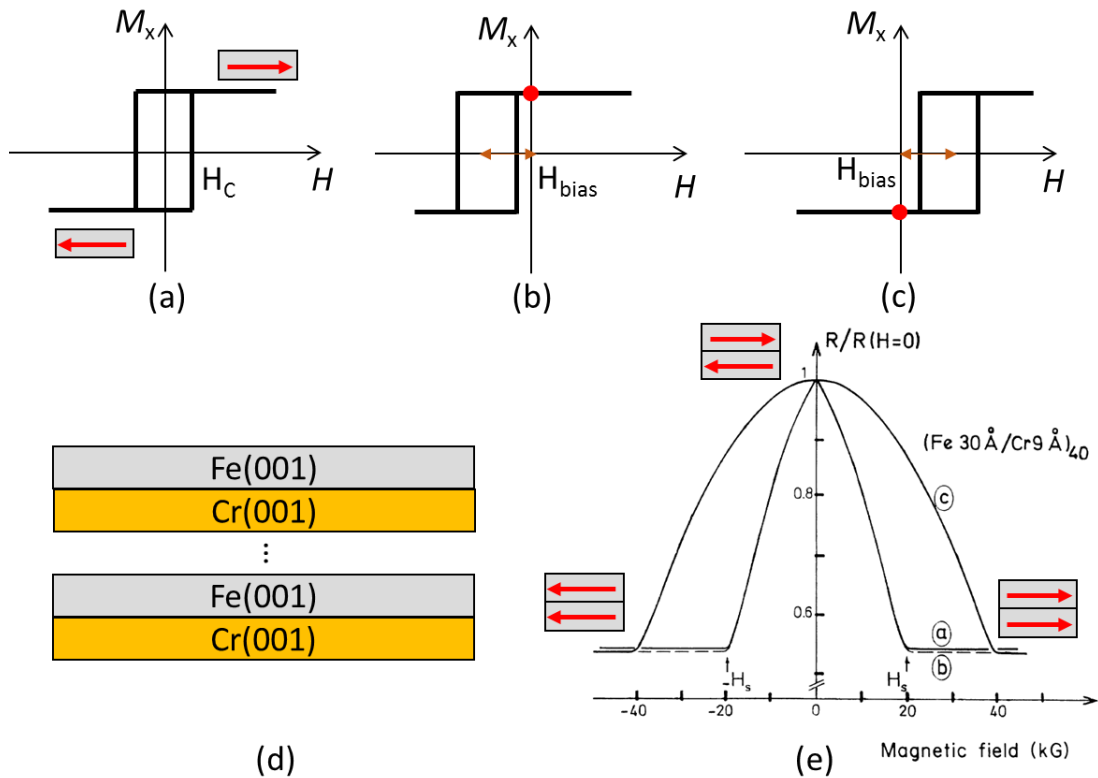


Figure 1-1 Ferromagnetic hysteresis with or without exchange bias and discovery of GMR in the Fe(001)/Cr(001) superlattice. (a) Normal magnetic hysteresis for a ferromagnet along the easy axis in the single domain regime. Inset is the illustration of easy axis along $\pm x$ direction. (b) Ferromagnetic hysteresis with a negative exchange bias through exchange coupling with an antiferromagnet. Red dot indicates that in the absence of external magnetic field, the magnetization is along $+x$ direction. (c) Ferromagnetic hysteresis with a positive bias. Red dot indicates that in the absence of external magnetic field, the magnetization is along $-x$ direction. (d) Schematic of the Fe(001)/Cr(001) superlattice used in the initial finding of GMR. (e) Magnetoresistance curves of a Fe/Cr superlattice at 4.2 K. The current is along [110] and the field is in the layer plane along the current direction (curve a), in the layer plane perpendicular to the current (curve b), or perpendicular to the layer plane (curve c). (e) is reprinted with permission from [3], Copyright 1988 by the American Physical Society.

Note that to control the resistance state, a large external magnetic field is required since the Cr layer pins both top and bottom Fe layer in the opposite fashion. Afterwards, MTJs are developed to realize resistance control using a relatively small field (see Figure 1-2a, only top layer is pinned). Ideal resistance hysteresis is given in Figure 1-2b. From scaling point of view, magnetic field is very hard to be integrated into electronic devices without hindering the scaling performance [4]. So, we do not want magnetic field to control the resistance state. In the next section, current and voltage control of the MTJ resistance state are discussed.

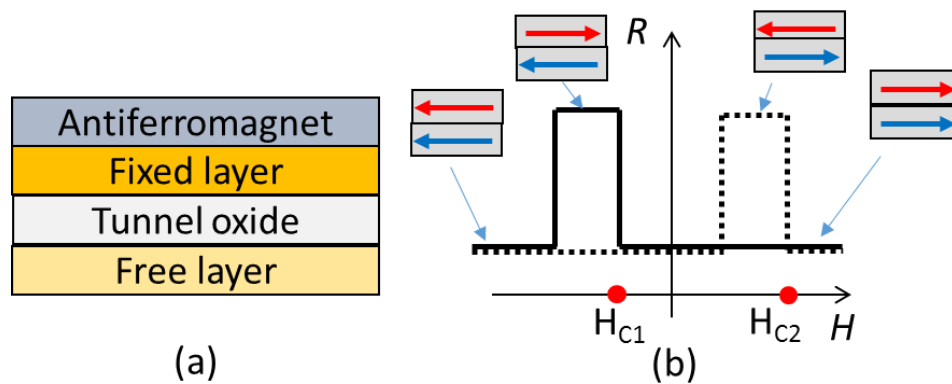


Figure 1-2 (a) Schematic of a MTJ. (b) Ideal resistance hysteresis when magnetic field is applied to a MTJ. H_{C1} and H_{C2} are the coercivity field for the free layer and the fixed layer, respectively.

1.2 Spin-transfer torque and voltage-controlled magnetic anisotropy

1.2.1 Spin-transfer torque

Spin-transfer torque (STT) was theoretically proposed in 1996 independently by J. C. Slonczewski [5] and L. Berger [6]. MRAM utilizing STTs is called STT-MRAM. When the spin-unpolarized current goes through a noncolinear spin valves or MTJs, a spin-transfer torque could be

generated to manipulate the magnetization state of the ferromagnet. Figure 1-3 describe the write operation of a MTJ using STTs, where the magnetization of the fixed layer is always spin right. If the initial state is 1, writing a 0 requires applying current from the fixed layer to the free layer. While the injection current is unpolarized, it becomes spin-right-polarized after the fixed layer due to the spin torque given by the magnetization of the fixed layer. This spin-right-polarized torque will give a STT on the magnetization of the free layer, forcing it flip after a certain threshold. If the initial state is 0, writing a 0 requires applying current from the free layer to the fixed layer. Similar to write a 1, carriers with spin-right will easily go through the tunnel oxide, and carriers with spin-left will mostly be scattered back. These back-scattering carriers with spin-left will exert a STT on the magnetization of the free layer and even flip it after a certain threshold current. From the operation principle, we see that the switching mechanisms of write 1 and write 0 are not the same, which gives generally different switching time and critical switching current. This asymmetry causes some issues in terms of reliability and circuit design complexity.

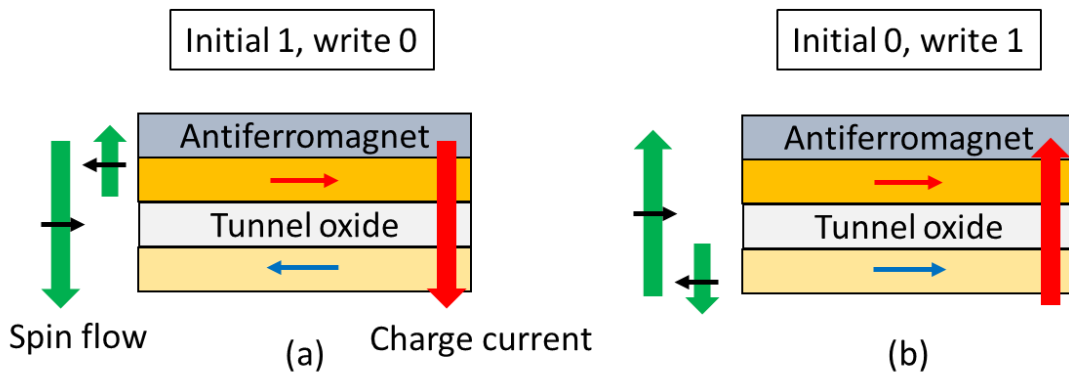


Figure 1-3 Illustration of write operation using spin-transfer torque. (a) Initial state is high resistance state (antiparallel state, 1). Applying charge current from fixed layer to free layer changes the state to low resistance state (parallel state, 0, not shown in the figure). Spin right goes through tunnel oxide (as a spin filter) more than spin left, and then generates torque on the magnetization of free layer. (b) Initial state is 0, and then write 1 (final state is also not shown in

the figure). Spin right goes through tunnel oxide more than spin left. Spin left bounces back and then generates torque on the magnetization of free layer.

To describe the dynamics of magnetization, we can use Landau–Lifshitz–Gilbert (LLG) equation:

$$\begin{aligned} \frac{d\mathbf{M}}{dt} &= \gamma \mathbf{M} \times \mathbf{H}_{eff} + \frac{\alpha}{M_s} \mathbf{M} \times \frac{d\mathbf{M}}{dt} \Leftrightarrow (1 + \alpha^2) \frac{d\mathbf{m}}{dt} \\ &= \gamma \mathbf{m} \times \mathbf{H}_{eff} + \alpha \gamma \mathbf{m} \times \mathbf{m} \times \mathbf{H}_{eff} \end{aligned} \quad (4)$$

where $\gamma = qg\mu_0/2m_e$ is the gyromagnetic ratio (for electron, it is negative and g -factor is around 2), $M_s = |\mathbf{M}|$ is the saturation magnetization, $\mathbf{m} = \mathbf{M}/M_s$ is the normalized magnetization vector, \mathbf{H}_{eff} is the effective magnetic field and α is a phenomenological damping parameter. At equilibrium, the magnetization direction is along the effective magnetic field. Here, the effective magnetic field includes external magnetic field, anisotropy field and demagnetization field, and could be written as $\mathbf{H}_{eff} = \mathbf{H}_{ext} + \mathbf{H}_{an} + \mathbf{H}_d$. Here, we do not focus on the discussion of these field, and good reference materials could be found in Ref. [4]. When additional STTs are present, the LLG equation is revised as:

$$\frac{1}{\gamma'} \frac{d\mathbf{m}}{dt} = \mathbf{m} \times \mathbf{H}_{eff} + \alpha \mathbf{m} \times \mathbf{m} \times \mathbf{H}_{eff} - I_{inj} \frac{\hbar P}{2\mu_0 e M_s A t} \mathbf{m} \times \mathbf{m} \times \mathbf{p} \quad (5)$$

where $\gamma' = \gamma/(1 + \alpha^2)$ is the reduced gyromagnetic ratio, $P = (J_{\uparrow} - J_{\downarrow})/(J_{\uparrow} + J_{\downarrow})$ is the STT polarization (it is generally different for write 1 and write 0), A is the area of free layer, t is the thickness of free layer and \mathbf{p} is the polarization vector. For normal ferromagnets, the damping factor is a positive value. When the injection current is larger than the critical current $I_{inj} > I_c = \frac{2\alpha\mu_0 e M_s A t H_{eff}}{\hbar P}$, the effective damping factor $\alpha_{eff} = \alpha - \frac{\hbar P I_{inj}}{2\mu_0 e M_s A t H_{eff}}$ becomes a negative value, and then magnetization vector precesses to the opposite direction compared with the case in the absence of injection current.

Tradition MTJs have in-plane easy axes due to the strong demagnetization field originated from the nature of thin film ferromagnetic layer. Thickness of the ferromagnetic layer is around several nanometers, which is much smaller compared with the lateral size (tens to hundreds of nanometers depending on the technology node). For in-plane MTJs, the critical switching current is given by [7]

$$I_c = \frac{2\alpha\mu_0 eM_s At}{\hbar P} \left(H_{k,eff} + \frac{H_d}{2} \right) \quad (6)$$

where $H_{k,eff}$ and H_d are in-plane effective anisotropy field and out-of-plane demagnetization field. Reduction of critical switching current is preferred, and In practice, by using partial perpendicular magnetic anisotropy (PMA), the critical switching current could be reduced according to $I_c = \frac{2\alpha\mu_0 eM_s At}{\hbar P} \left(H_{k,eff} + \frac{H_d - H_{\perp}}{2} \right)$, where H_{\perp} is the partial perpendicular effective anisotropy field [7].

Ultimately, for perpendicular MTJs, the critical switching current is given by

$$I_c = \frac{2\alpha\mu_0 eM_s At H_{k,eff}^{\perp}}{\hbar P} \quad (7)$$

where $H_{k,eff}^{\perp}$ is the out-of-plane effective anisotropy field. Reduction of switching current using PMA has already been demonstrated experimentally [8, 9].

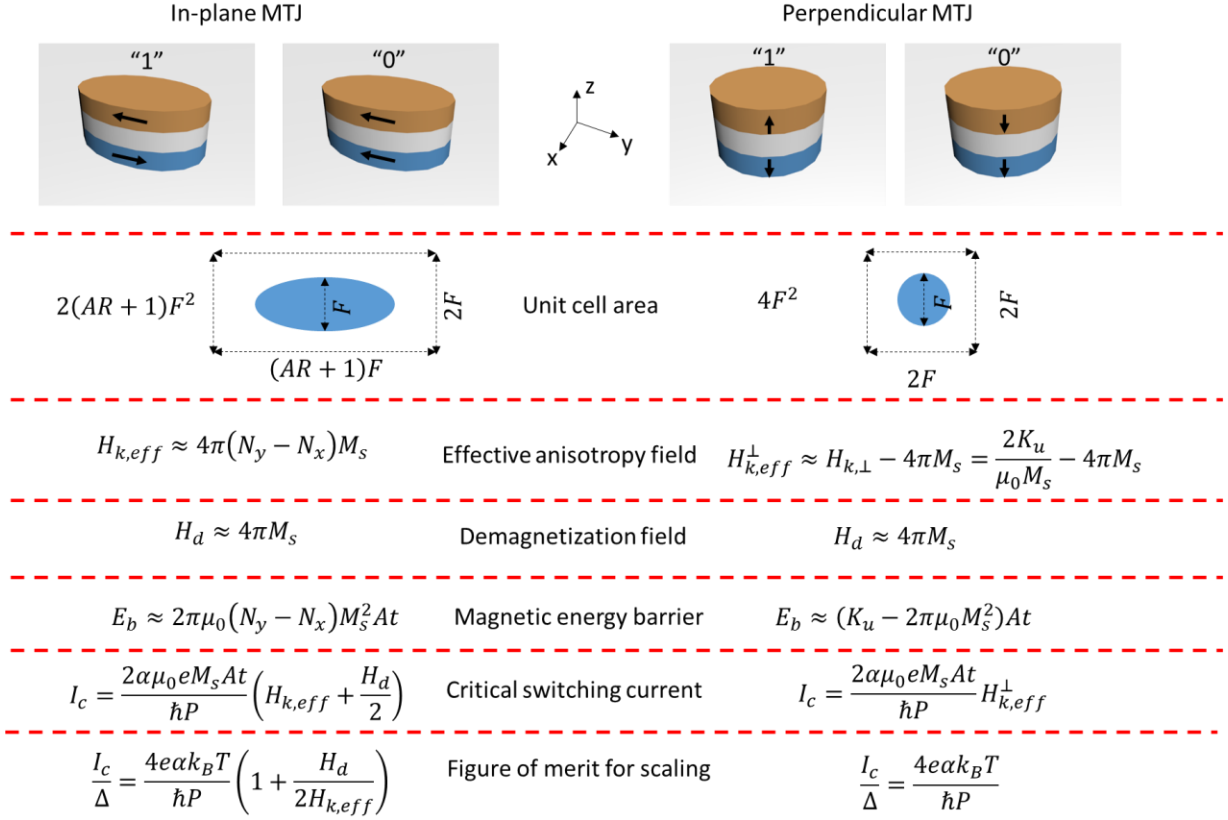


Figure 1-4 Comparison of in-plane and perpendicular MTJs. AR is the aspect ratio. For details, see section 1.4 in Ref. [4].

1.2.2 Voltage-controlled magnetic anisotropy

For iron-riched CoFeB/MgO interface, there is a strong interfacial perpendicular anisotropy that could overcome the demagnetization field and make the free layer have out-of-plane easy axis [9]. In this case, the anisotropy energy density and corresponding perpendicular anisotropy field are given by

$$K_\perp = \frac{S_i}{t} - 2\pi\mu_0 M_s^2, \quad H_{k,eff}^\perp \approx \frac{2S_i}{\mu_0 M_s t} - 4\pi M_s \quad (8)$$

where S_i is the interfacial anisotropy energy originated from CoFeB/MgO interface. So, when the thickness of CoFeB layer is smaller than a certain value, the out-of-plane anisotropy energy becomes positive, indicating a perpendicular anisotropy.

Before talking about the write mechanism in perpendicular MTJs, we first define the thermal stability here. Thermal stability is the first requirement for any kind of MRAM, and it indicates the ability to against the thermal perturbation in the ambient environment. It is defined as the magnetic energy barrier over thermal excitation energy: $\Delta = E_b/k_B T$, where E_b is the magnetic energy barrier, k_B is the Boltzmann constant and T is the temperature. For a single MTJ, Δ should be larger than 40 to achieve 10 years retention time (time scale that information stored does not lose). In addition, to fulfill a certain retention time requirement, one also needs to consider the memory density. If the density of MTJs is high, the variability and disturbance between bits will require higher Δ . For example, for dense memory application (> 16 MB), Δ should be larger than 70 for a ten-year retention time [10]. Magnetic energy barrier is the energy required to overcome to flip the magnetization from one easy axis to the other axis (here MTJs with only two easy axes are considered). For in-plane MTJs that magnetic anisotropy is defined by the shape, they have two easy axes along the long axis of the ellipse ($\pm y$ direction in Figure 1-4). For perpendicular MTJs that magnetic anisotropy is given by the interfacial anisotropy, they have two easy axes along the direction perpendicular to the film plane ($\pm z$ direction in Figure 1-4). As shown in Figure 1-4 and section 1.4 in Ref. [4], thermal stabilities for in-plane MTJs and perpendicular MTJs are given by

$$\Delta_{\text{in}} = \frac{2\pi\mu_0(N_y - N_x)M_s^2 A t}{k_B T}, \quad \Delta_{\text{p}} = \frac{(K_u - 2\pi\mu_0 M_s^2) A t}{k_B T} = \frac{S_i A - 2\pi\mu_0 M_s^2 A t}{k_B T} \quad (9)$$

So, to keep the target retention time (almost a constant Δ), aspect ratio (N_y/N_x), thickness of the free layer t and/or saturation magnetization M_s should be increased for in-plane MTJs. On the other hand, for perpendicular MTJs, only interfacial anisotropy K_u (S_i) should be increased and saturation magnetization M_s and the thickness of the free layer t should be reduced.

Voltage-controlled magnetic anisotropy (VCMA) effect is observed in the iron-riched CoFeB/MgO system [11]. The voltage-dependent perpendicular anisotropy can be written as

$$K_{\perp} = \frac{S_i - \xi V/d_{ox}}{t} - 2\pi\mu_0 M_S^2 \quad (10)$$

where ξ is the VCMA coefficient and d_{ox} is thickness of the tunnel oxide. VMCA effect could be used as an energy efficient switching mechanism compared with STTs. MRAM utilizing VCMA effect is called magnetoelectric RAM (MeRAM) in this thesis. There are two possible mechanisms that contribute to the VCMA effect: electric-field modulation of orbital occupation [11] and electric-field controlled Rashba spin-orbit anisotropy [12]. Details could be found in section 2.3 in Ref. [4].

To compare STT-MRAMs and MeRAMs in terms of energy efficiency and scalability, we define the following figure of merits:

$$\frac{I_c}{\Delta} = \frac{4e\alpha k_B T}{\hbar P}, \quad \frac{V_c}{\Delta} = \frac{k_B T d_{ox}}{A\xi} \quad (11)$$

These two factors, ratio of critical switching current or voltage over the thermal stability, measure the relative ability to switching a perpendicular MTJ (MEJ). The smaller I_c/Δ (V_c/Δ) is, the lower current (voltage) is required to realize switching if the thermal stability is kept as a constant. For I_c/Δ , it is fundamentally limited by some physical constants, and to improve the scaling performance, the ratio of damping factor to STT polarization α/P has to be reduced. In practice, these two parameters are the properties of materials, and are limited in a certain range right now. So, as the device scales down, the current remains a constant if the thermal stability keeps constant. However, since MTJ area reduces, the current density will increase a lot and cause serious problems, such as high power dissipation and Joule heating induced reliability issue. For V_c/Δ , as the device scales down, the voltage also increases if the thermal stability and the VCMA coefficient are kept as constants. This is not realistic, since increase of voltage will also cause similar problems as in STT-MRAMs. So, increase of VCMA coefficients is required. Indeed

several methods and new materials are discovered and studied to fulfill the requirement of high VCMA coefficients. If we could keep $A\xi$ a constant, the voltage will remain as a constant. As the device scale down, the resistance of MEJs will increase and then reduce the leakage current and corresponding power dissipation. From this simple analysis, we see that electric-field control of magnetism, in principle, has better scaling potential in terms of energy efficiency.

1.3 Spin-orbit torque

1.3.1 General expression for spin-orbit torque and Hall resistance

The Hall measurement is very important for quantitatively determining the transport properties of semiconductors, such as carrier density and Hall mobility. The schematic of set-up is drawn in Figure 1-5a. The current is along $\pm y$ direction, and the direction of external magnetic field is described by two angles: polar angle θ and azimuthal angle φ . Magnetoresistance and Hall resistance are measured using four-probe technique. For magnetic materials, when the magnetic field is applied perpendicular to the film plane, the general expression is given by [13]

$$R_{\text{Hall}} = R_{\text{AHE}} + R_{\text{OHE}} = R_{\text{A}} m_z + R_0 H_z \quad (12)$$

where R_{AHE} and R_{OHE} are the Anomalous Hall Effect (AHE) resistance and ordinary Hall Effect (OHE) resistance, respectively and R_0 and R_{A} are the OHE coefficient and AHE coefficient, respectively. For a nonmagnetic semiconductor, such as silicon and germanium, the $R_{\text{Hall}} - H$ curve is linear (see Figure 1-6), and the carrier density is given by $n = \frac{1}{|q|R_0}$ and Hall mobility is given by $\mu_n = R_0 \sigma_n$, where σ_n is the conductivity of sample. For a magnetic semiconductor, such as (Ga,Mn)As, MnGe, Cr-(Bi_xSb_{1-x})Te₃ at low temperature, the $R_{\text{Hall}} - H$ curve will develop a hysteresis, since there is a ferromagnetic phase inside (see Figure 1-6). Here, MnGaAs and MnGe are diluted magnetic semiconductors (DMSs). Cr-(Bi_xSb_{1-x})Te₃ is a magnetic topological insulator (TI), and it will be the main focus in Chapter 2 and Chapter 3. For a metal, typically the

OHE can be ignored thanks to negligible OHE coefficient originated from large carrier density. So, if the sample is a ferromagnetic metal, the $R_{\text{Hall}} - H$ curve will be dominated by the AHE.

From above discussion, we see that R_{Hall} can be a good parameter for obtaining m_z under the single domain approximation. Here, single domain approximation assumes that the total magnetization of the sample rotates coherently as one giant magnetic moment. This assumption is typically reasonable for around or below micrometer size sample or sample subject to large magnetic field. In a small sample, it behaves intrinsically like a nanomagnet, and its magnetic moments behave collectively. Under a large magnetic field, all magnetic domains will be aligned along the external magnetic field and then all magnetic moments behave like a huge magnetic moment.

If the external magnetic is not along the perpendicular direction, there will be a component originated from planar Hall Effect (PHE) resistance [14, 15]. The direction of external magnetic field is described by a polar angle θ and an azimuthal angle φ . PHE is an effect that when the magnetic field is applied in the film plane, there is also a transverse voltage signal generated. It is originated from anisotropy magnetoresistance (AMR) of magnetic materials. Typically, $R_{\text{PHE}} = R_{\text{P}}m_xm_y$, where R_{P} is the PHE coefficient, m_x and m_y are the direction vector x and y component, respectively (see Figure 1-6). Here, R_{P} is defined as resistance change relative to the resistance when the external magnetic field and injection current are along the +y direction. Therefore, for a magnetic material under external magnetic field, the total Hall resistance could be written as

$$R_{\text{Hall}} = R_0H_z + R_A m_z + R_{\text{P}}m_xm_y \quad (13)$$

From Eq. 13, we know that from systematic Hall measurement, the magnetization direction vector could be determined. Further, we can study the effect of current-induced spin torque on the magnetization. There are two basic types of current-induced spin torque: field-like torque and damping-like torque (see Figure 1-5b). For field-like torque, $\tau_F = m \times p_f$, where p_f is the field-like

field induced by injection current. For a given injection current, the field-like field is fixed. For damping-like torque, $\tau_D = m \times m \times p_d$, where $m \times p_d$ is the damping-like field induced by injection current. For a given injection current, the damping-like field also depends on the magnetization itself.

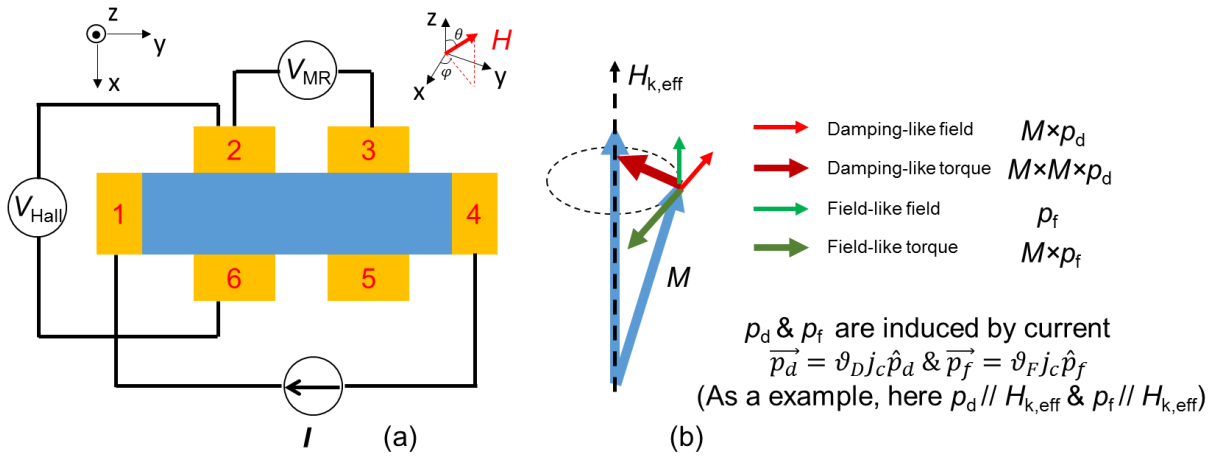


Figure 1-5 Hall bar measurement set-up and two types of spin-orbit torques (fields). (a) Schematic of six-probe Hall-bar measurement system. The direction of magnetic field is described by two angles: polar angle θ and azimuthal angle φ . (b) Two types of spin-orbit fields: damping-like field not only depends on the injection current, but also depends on the magnetization, but field-like field only depends on the injection current. In the linear response regime, p_d & p_f are proportional to the current density, but their directions depend on the specific materials and structures.

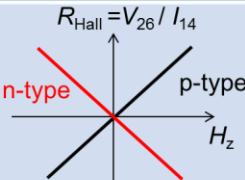
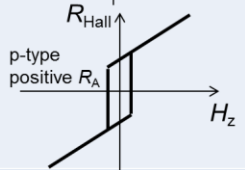
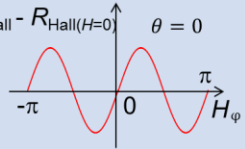
	Origin	Expression	Typical characteristic
(Ordinary) Hall Effect	Deflection due to Lorentz force	$R_{\text{OHE}} = R_0 H_z$	
Anomalous Hall Effect	In magnetic system with spin-orbit interaction: Intrinsic deflection due to Berry' phase; Side jump; Skew scattering	$R_{\text{AHE}} = R_A m_z$	
Planar Hall Effect	Anisotropic magnetoresistance	$R_{\text{PHE}} = R_P m_x m_y$	
Spin Hall Effect	In nonmagnetic system with spin-orbit interaction: Same as AHE, but without charge accumulation	$J_S = \vartheta_{\text{SHE}} J_C$	
Topological Hall Effect	Presence of skyrmion		

Figure 1-6 Summary of different kinds of Hall Effect: origin, expression and typical characteristic.

The above definition of two types of spin torque is comprehensive, but not specific. From the theoretical discovery of STT in 1996, all spin torques can be fallen into these two categories. For example, STT is a typical damping-like torque, since it has double cross-product of magnetization (see the last term in Eq. 5). Later on, in magnetic systems with heavy elements, Rashba spin-splitting induced spin torque and Spin Hall Effect (SHE) induced STT are discovered in series. I will introduce these two spin torques in the next section.

1.3.2 Rashba effect and Spin Hall Effect

To my knowledge, the current-induced magnetization switching using other spin torques rather than STTs was first observed in DMS systems, in a (Ga,Mn)As thin microdisk in 2009 [16]. (Ga,Mn)As is a p-type ferromagnetic semiconductor with zinc-blende crystalline structure similar

to GaAs (see Figure 1-7a). There is a strong Rashba spin-orbit interaction inside (Ga,Mn)As, as shown in Figure 1-7b. When passing electron current through +x direction, an unbalanced spin accumulation along +y direction will be induced by this Rashba spin-orbit interaction. The easy axes are in the film plane along [100] and [010] direction as shown in Figure 1-7c. When current is passed along [110] direction, the effective spin-orbit magnetic field is generated along $[\bar{1}10]$ direction. If the current is along opposite direction of [110], the effective spin-orbit magnetic field will also become along opposite direction of $[\bar{1}10]$. Therefore, the magnetization could be reoriented between easy axes [010] and [100] using the injection current. This magnetization reorientation could be read out through AMR.

However, the anisotropy energy for these in-plane easy axes is not strong enough at room temperature, as the experiments were conducted at low temperature [16]. Then, information stored inside the magnetization state can be easily lost under the perturbation of thermal excitation. In 2010 and 2011, magnetization switching driven by current-driven domain wall motion and current-induced Rashba spin torque in single domain regime were subsequently demonstrated by Ioan Mihalai Miron et al. [17, 18]. Here, the material system is Pt/Co/AIO_x with perpendicular magnetic anisotropy (PMA). Similar to iron-riched CoFeB/MgO system, Co/AIO_x also gives a very strong PMA. Current-induced domain wall motion and single domain switching in Pt/Co/AIO_x nanoribbon and nanodot are studied in Ref. [18] and Ref. [17]. Here, we focus on single domain switching Pt/Co/AIO_x nanodot (500nm × 500nm). By passing current along ±y direction through Pt/Co/AIO_x trilayer structure (see Figure 1-8a), the Rashba-field is induced due to structure asymmetry. Note that Rashba-field is a field-like field along ±x direction (see Figure 1-8b-c) induced by the injection current, but it cannot give deterministic magnetization switching from up to down or from down to up by itself even in the presence of external magnetic field. In this paper, authors argued that this Rashba-field can also give rise to a damping-like field along the z direction based on symmetry argument, which uniquely determine the final magnetization

state. As shown in Figure 1-8c, magnetization rotates from down to up in an anticlockwise fashion in the presence of external magnetic along +y direction. Only final magnetization state is given in Figure 1-8c, and at any time during magnetization reversal, damping-like field always follows $m \times H_F$. When the magnetization is along external magnetic field direction, damping-like field points up, which gives rise to the final state. Since external magnetic field breaks mirror symmetry, injection current determines the final state. If there is no external magnetic field as shown in Figure 1-8b, damping-like field will continuously rotate the magnetization in an anticlockwise fashion, and there is no difference between real world and world in mirror, that both up and down are allowed. So, mirror symmetry-breaking field is required to achieve deterministic switching. However, as we said before, external magnetic field really hurts the real applications and scaling performance. In magnetization switching experiments done by Guoqiang Yu et al. [19], lateral structure asymmetry along x direction is induced to introduce additional field-like field along z direction due to different oxide state. This additional field-like field along z direction also breaks the mirror symmetry, which give rise to a deterministic switching.

Later on, in the (almost) same system, Luqiao Liu et al. [20, 21] argued that Spin Hall Effect (SHE), instead of Rashba effect proposed by Ioan Mihai Miron et al. [17, 18], is the true reason behind the magnetization switching. Principles of SHE are the same as AHE (see Figure 1-6), and the only difference is that SHE happens in nonmagnetic systems, and only gives spin accumulation in the transverse direction, not charge accumulation (no transverse voltage can be detected). As shown in Figure 1-7d, in the ferromagnet/heavy metal heterostructure, electrons with spin pointing to -x direction go up under -y direction electric field and this deflected spin current gives rise to a spin-transfer-like torque on the magnetic moment of adjacent magnetic layer. SHE induced spin torque can also be thought as a current-induced damping-like field on the magnetization. So, even without Rashba field (field-like field), the trilayer system could be switched as long as the damping-like field exists and an external magnetic field is applied to break the symmetry. All these

arguments are confirmed by the giant SHE in heavy metals, such as Pt and Ta. Moreover, since Pt and Ta have opposite spin Hall angle, they prefer different switching direction and this is also experimentally verified [20, 21]. Therefore, scientific communities are kind of drawing conclusion that SHE is the real reason behind this magnetization switching in oxide/ferromagnet/heavy metal trilayers.

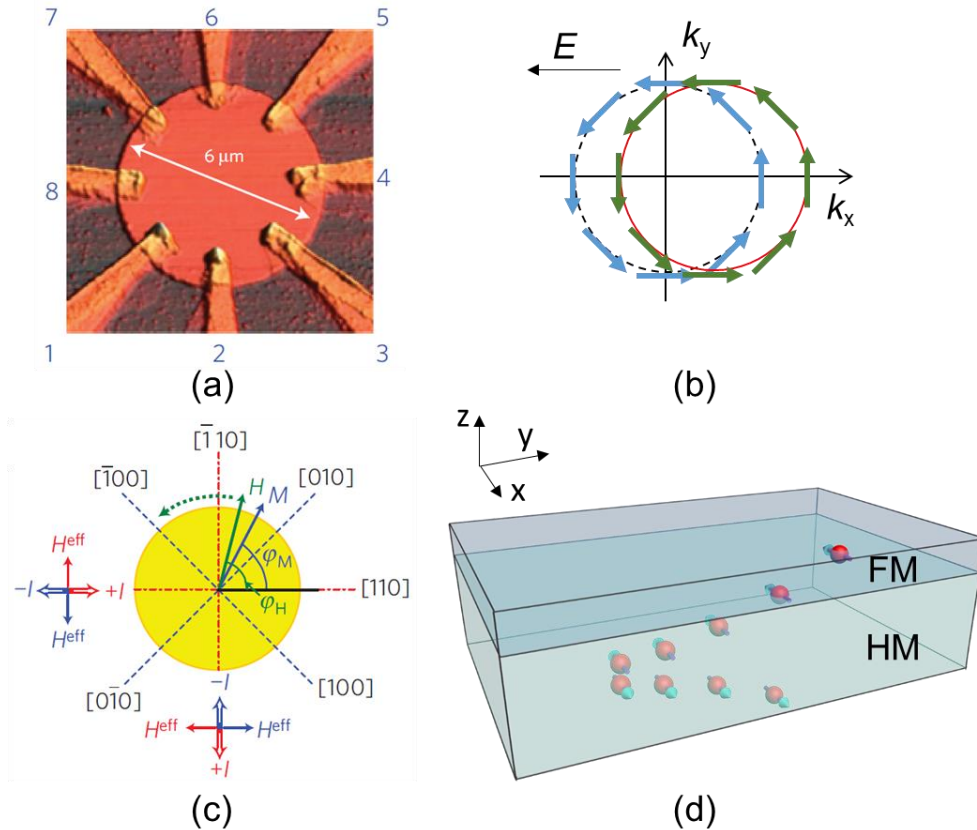


Figure 1-7 Rashba spin-orbit interaction and SHE in heavy metal/ferromagnet heterostructures. (a) AFM picture of (Ga,Mn)As disk. (b) Rashba-type spin-splitting band in a p-type ferromagnetic semiconductor. Here, the spin direction rotates along the Fermi surface circle in an anticlockwise fashion. Under electric field along $-x$ direction, a net momentum of electrons along $+k_x$ direction will induce spin accumulation along $+y$ direction. (c) Diagram of device orientation with respect to crystallographic axes, with easy and hard magnetization axes marked with blue dashed and red dot-dash lines, respectively. Measured directions of H_{eff} field are shown for different current

directions. (d) SHE induced spin deflection in ferromagnet/heavy metal heterostructures. In this heavy metal, electrons with spin along $-x$ direction will deflect to $+z$ direction and electrons with spin along $+x$ direction will deflect to $-z$ direction. Electrons with spin along $-x$ direction will induce a spin torque on the magnetization of the above ferromagnet. (a) and (c) are reprinted by permission from Macmillan Publishers Ltd: Nature Physics [16], copyright 2009.

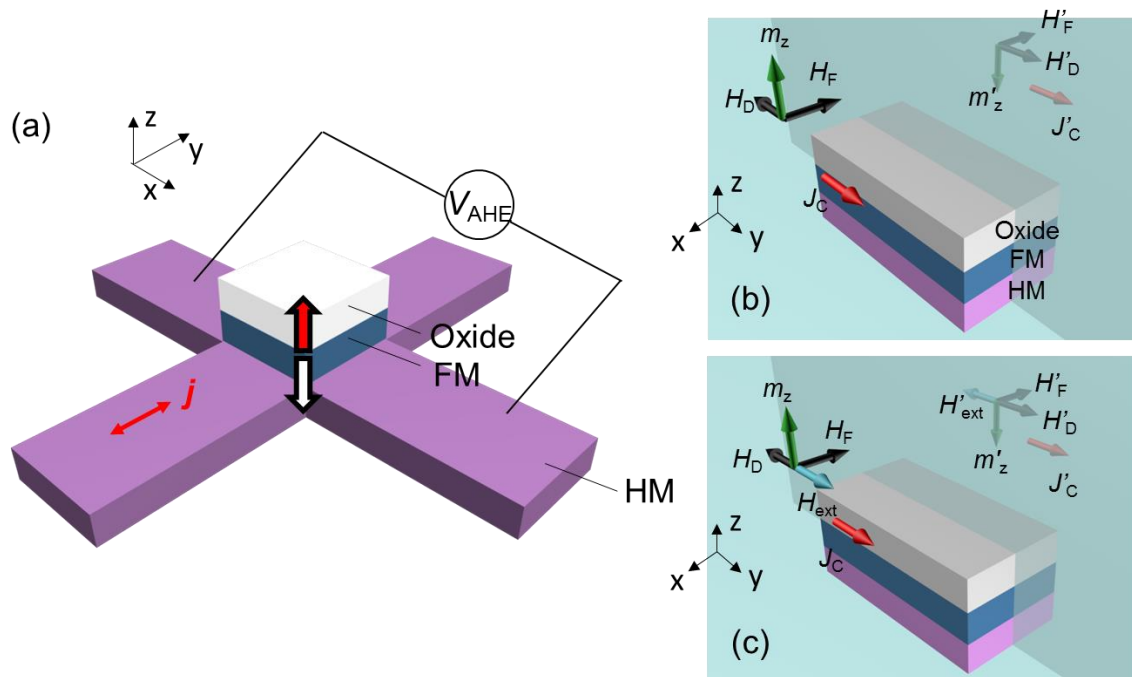


Figure 1-8 Prototype of current-induced PMA switching device and general principle of switching mechanism in terms of mirror symmetry breaking. (a) Schematic of the oxide/ferromagnet metal/heavy metal trilayer structure. The current is applied in the $\pm y$ direction, and m_z is measured through the AHE resistance. (b) Mirror symmetry of the trilayer system. The system obeys mirror symmetry, and then we can directly see that injection current along $+y$ direction allows both up and down magnetization state. (c) Mirror symmetry breaking of the trilayer system in the presence of external magnetic field. Here, injection current along $+y$ direction only allows up magnetization state, and current along $-y$ direction allows down magnetization state.

The competition between these two effects never ends. More recently, a lot of evidences indicate that field-like field induced by current is also very important. As we discussed before, field-like field along z direction is introduced by different oxide states to achieve a deterministic switching in the absence of external magnetic field [19]. Systematic measurement shows that field-like torque and damping-like torque can be in the same order, and high-order terms may also play a role in the magnetization switching [4, 14]. By engineering the interface between Pt/CoFeB/MgO using oxidation, the switching direction could be changed, even the spin Hall angle of Pt keeps the same; that indicates an another spin torque beyond SHE induced torque [22]. All these evidences draw a conclusion, in my opinion, that both field-like torque and damping-like torque exist and contribute in current-induced magnetization switching systems, and careful study and engineering are really the keys to make the magnetic system smarter and more efficient.

1.3.3 Spin-orbit torque MRAM

In this thesis, we refer all kinds of spin torque except STT as spin-orbit torque (SOT). The key for SOT is spin-orbit coupling (SOC), and the SOT is generated by the spin-unpolarized current. In contrast, by passing current through a ferromagnet, injection current becomes spin-polarized current and then gives rise to a STT on the magnetization of next ferromagnet.

One of most important applications for SOTs is SOT-MRAM (see Figure 1-9). SOT-MRAM utilizes SOTs generated by heavy metals or other SOC source to switch the free layer of a MTJ. The switching current relationship between SOT-MRAMs and STT-MRAMs is given by [4, 23]

$$\frac{I_{\text{SOT}}}{I_{\text{STT}}} \approx \frac{P}{\vartheta_{\text{SOT}}} \frac{A_{\text{SOC}}}{A_{\text{MTJ}}} \quad (14)$$

where ϑ_{SOT} is spin torque ratio, A_{SOC} and A_{MTJ} are the cross-section area of the SOC layer and the MTJ, respectively. ϑ_{SOT} is the most important parameter we will pursue in this thesis, and it is an indicator of how much torque could be generated per unit current density. ϑ_{SOT} could be written as

$$\vartheta_{\text{SOT}} = \frac{J_s}{J_c} = \frac{2eM_s t B_{\text{SO}}}{\hbar J_c} \quad (15)$$

So, to reduce the switching current, increase the area ratio of $A_{\text{MTJ}}/A_{\text{SOC}}$ and increase ϑ_{SOT} are important. Since the reduction of thickness of SOC layer will increase the resistance of the SOC layer, increase of ϑ_{SOT} becomes more practical. The SOT-MRAM has its own advantages: symmetrical switching mechanism, potentially lower switching current and higher endurance, since the current is not directly passed through MTJs. However, SOT-MRAMs also have an obvious drawback: it is a three-terminal device, that increases the design and area cost.

Since ϑ_{SOT} is so important for SOT-MRAM, we try to find a better material with higher ϑ_{SOT} in this thesis. As the title indicates, topological insulators (TIs) are our choice. We find that ϑ_{SOT} of topological insulators is huge compared with heavy metals. And we design different structures to study the origin of this giant ϑ_{SOT} . In next section, I briefly introduce the outline of this thesis.

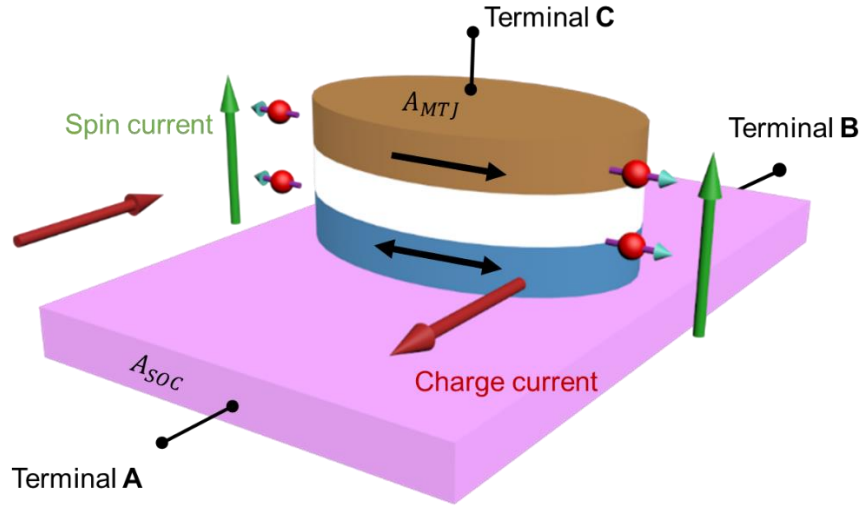


Figure 1-9 Spin-orbit torque MRAM. The SOC layer has large spin torque ratio and efficiently generate SOTs to switch the magnetization of the free layer. The magnetization state of the free layer can be read out through the resistance state of the MTJ (terminal A-C or B-C). The injection current used to write is passed through terminal A-B.

1.4 Thesis outline

In Chapter 2, we firstly study the SHE induced SOTs in heavy metal/ferromagnet heterostructures, especially in Ta/CoFeB/MgO. We use the second harmonic ac lock-in technique to quantitatively measure the spin torque ratio. Then, we introduce TIs and use the same method to study the spin torque in TI-based Cr-TI (chromium-doped topological insulator) single layer and Cr-TI/TI bilayer structures. This chapter deals with detailed measurement and analysis, which is the key for accurately extracting ϑ_{SOT} . In the same time, we demonstrate that spin torque ratio of TIs is giant compared with that of heavy metals.

In Chapter 3, we design different heterostructures including TI/Cr-TI/TI trilayer structures and use electric-field to control surface states of the Cr-TI single layer to show that surface state induced

SOTs are probably the most important for TI related magnetization switching experiments. This chapter explores the mechanism of this giant SOT in TIs.

In Chapter 4, we briefly summarize all important things discussed above and give a perspective of next step in TI-based SOT study.

Chapter 2. Spin-orbit torque in heavy metals and topological insulators

In this chapter, we first reproduce the results of SOT study in Ta/CoFeB/MgO in section 2.1, and obtain consistent results to show that our second harmonic technique is accurate. Then, in section 2.2, we use similar technique to measure SOTs in the TI/Cr-TI bilayer and the Cr-TI single layer, and show that the magnitude of SOT in TI systems is much larger than the case in heavy metals. After demonstration of giant SOT in TIs, we are ready to see the current-induced magnetization switching in Cr-TIs with a very low threshold current in section 2.3.

2.1 Heavy metal/ferromagnet heterostructure for SOT study

2.1.1 Harmonic analysis for SOT study

Ta/CoFeB/MgO is a well-studied SOT system, and the spin Hall angle of Ta is around 0.15 [20, 24]. Ta has opposite spin Hall sign compared with Pt [21, 25]. Here, we use Ta(6)/CoFeB(1)/MgO(thick) Hall bar device with channel width 20um, where the number inside brackets is the thickness of corresponding layer in nanometer. Schematic of the measurement set up is given in Figure 2-1a (only one pair of Hall bars are shown). The film is in the xy plane and the current is applied along $\pm y$ direction (positive current is along +y direction). The out-of-plane magnetic hysteresis is given in Figure 2-1b. We apply a small AC current with a RMS value magnitude of 1mA, and then measure the first-harmonic Hall (transverse) resistance. The AC current frequency used in this thesis is 15.85 Hz, unless specifically stated otherwise. The four-probe harmonic measurement has an advantage of high accuracy, since it eliminates the contact resistance and identify small signal in the large background. The applied current is $I(t) = \sqrt{2}I_{\text{RMS}} \sin(\omega t)$. The general expression of voltage is given by

$$V(t) = V^0 + \sqrt{2}V^{1\omega} \sin(\omega t) + \sqrt{2}V^{2\omega} \sin(2\omega t) + \text{high order terms} \quad (16)$$

where V^0 , $V^{1\omega}$ and $V^{2\omega}$ are the DC, first-harmonic and second-harmonic voltage (RMS value read by SR830 lock-in amplifiers, independent of time). So, the first-harmonic resistance and the second-harmonic resistance are given as $R^{1\omega} = V^{1\omega}/I_{\text{RMS}}$ and $R^{2\omega} = V^{2\omega}/I_{\text{RMS}}$ (independent of time). The first-harmonic resistance here is the same as the DC measurement case (apply DC current and measure the DC voltage). So, from the out-of-plane magnetic hysteresis loop, we know that the AHE coefficient is $R_A = 4.5\Omega$. (The overall offset of first-harmonic signal ($\sim 0.5\Omega$) is due to misalignment of Hall bar.) Since the carrier density in metallic Ta/CoFeB/MgO system is very high, the ordinary Hall resistance is negligible here. This is justified since the first-harmonic resistance is very flat after the magnetic field-induced switching.

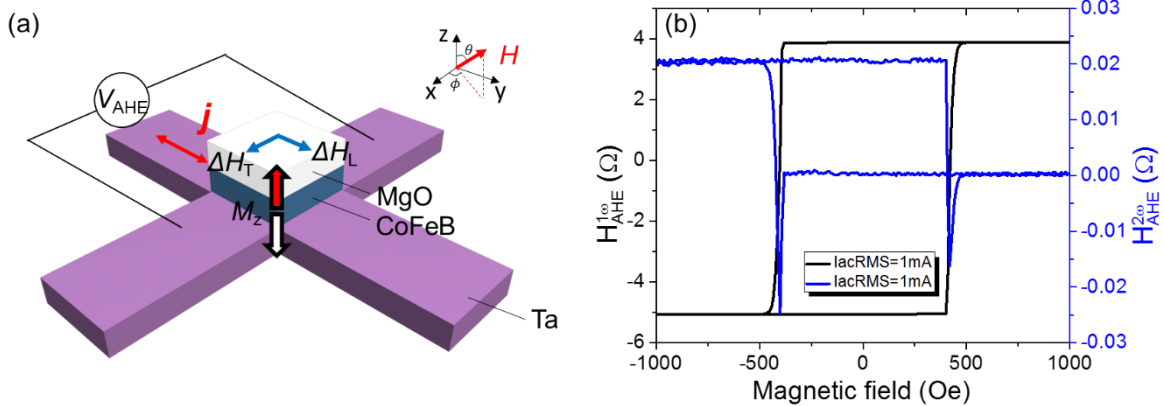


Figure 2-1 Schematic and out-of-plane magnetic hysteresis of Ta/CoFeB/MgO device. (a) Current is applied along $\pm y$ direction, and film is in the xy plane. External magnetic field is applied with polar angle θ and azimuthal angle ϕ . The current with generate longitudinal (damping-like) effective spin-orbit field ΔH_L and transverse (field-like) effective spin-orbit field ΔH_T . (b) Out-of-plane magnetic hysteresis (first-harmonic resistance) and second-harmonic resistance as a function of out-of-plane magnetic field for the Ta/CoFeB/MgO device. The film has a perpendicular magnetic anisotropy. The applied AC current magnitude (RMS value) is 1mA.

Second-harmonic signal can be used to detect the current-induced spin-orbit fields and thus spin-orbit torques. Here, we only consider the current-induced longitudinal spin-orbit field ΔH_L , since it is a damping-like field and determines the switching direction as we illustrated in Figure 1-8c. The direction of ΔH_L depends on the magnetization, $m \times x$. This is different from ΔH_T , which is a field-like field and points along $\pm x$ direction. To switch the ferromagnet, we need to apply the in-plane magnetic field along $\pm y$ direction and then apply DC current. To study the SOT, we first initialize the magnetization either in up or down state and then apply small magnetic field and small AC current along $\pm y$ direction. This AC current will generate second-harmonic resistance, which is directly related to the longitudinal spin-orbit field.

The existence of second harmonic signal indicates that the resistance also has a similar current dependence as applied AC current. The expression of current-dependent resistance can be written as $R^{2\omega}(t) = -2R^{2\omega} \sin(\omega t)$, where $R^{2\omega}(t)$ is proportional to $I(t)$. Then, the second-harmonic voltage signal is $\sqrt{2}V^{2\omega} \cos(2\omega t) = -2\sqrt{2}I_{\text{RMS}} \sin(\omega t) \cdot R^{2\omega} \sin(\omega t) + \sqrt{2}V^{2\omega} = \sqrt{2}V^{2\omega} \sin\left(2\omega t + \frac{\pi}{2}\right)$. So, we should pick up the out-of-phase second-harmonic voltage signal for calculating the second-harmonic resistance. The expression given in Eq. 16 is general and in the following, we consider the harmonic analysis of anomalous Hall resistance.

We first apply large +z direction magnetic field to align the magnetic moments along +z direction, and the first Hall resistance is given by $R_{\text{AHE}}^{1\omega} = R_A$. When we apply small magnetic field along $\pm y$ direction, the magnetization will be slightly tilted by a tilting angle θ due to the current-induced longitudinal spin-orbit field ΔH_L . The ΔH_L is along $\pm y$ direction, and it is a damping-like field. Here, we define +y direction is the positive direction of longitudinal spin-orbit fields for positive current (along +y direction). The tilting angle is given by $\theta(I) = \frac{H_y + \Delta H_L \sin \omega t}{H_k}$, where H_y is the external magnetic field along y direction and H_k is the effective magnetic anisotropy field along z direction (a constant depending only on the magnetic property of CoFeB/MgO). So, the Hall resistance is

given by $R_{\text{AHE}}(t) = R_{\text{AHE}}^{1\omega} - 2R_{\text{AHE}}^{2\omega} \sin(\omega t) = R_A \cos \theta \approx R_A \left(1 - \frac{\theta^2}{2}\right) = R_A \left(1 - \frac{H_y^2 + 2H_y \Delta H_L \sin \omega t}{2H_k^2}\right)$. So,

$R_{\text{AHE}}^{1\omega} = R_A \left(1 - \frac{H_y^2}{2H_k^2}\right)$ and $R_{\text{AHE}}^{2\omega} = \frac{R_A}{2} \frac{H_y \Delta H_L}{H_k^2}$. To calculate the current-induced longitudinal spin-orbit field, we just use formula:

$$\Delta H_L = -2 \frac{\partial R_{\text{AHE}}^{2\omega} / \partial H_y}{\partial^2 R_{\text{AHE}}^{1\omega} / \partial^2 H_y} \quad (17)$$

This is similar with the Eq. (1) in Ref. [24]. The experimental data is shown in Figure 2-2 for two different AC currents, 1mA and 0.5mA. The first-harmonic resistance is quadratic and the second-harmonic resistance is linear. From the fitting, we obtain that the current-induced spin-orbit field is around 1.67Oe for 0.5mA and 3.54Oe for 1mA. In terms of current density, efficiency of current-induced spin-orbit field is around $4.676 \times 10^{-6} \text{Oe}/(\text{A}/\text{cm}^2)$ at 0.5mA and $4.956 \times 10^{-6} \text{Oe}/(\text{A}/\text{cm}^2)$ at 1mA. There is still difference at different current levels, and it indicates that current-induced spin-orbit field may not be perfectly proportional to the current density, and there are possibly higher order terms. In this thesis, we only consider current-induced SOTs the linear regime, considering that this difference may also be due to the high noise level at small current case.

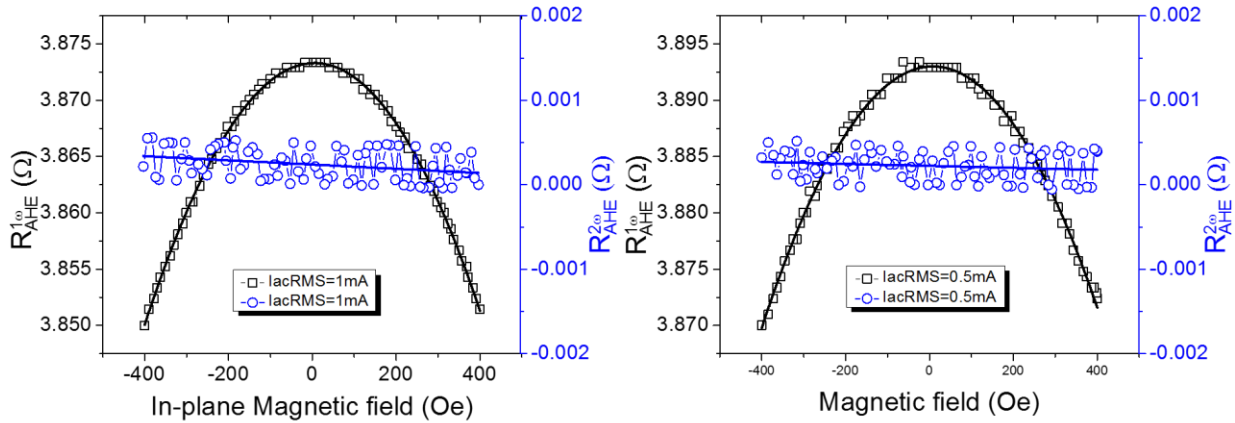


Figure 2-2 First-harmonic and second-harmonic measurement for calculating the current-induced (out-of-plane) longitudinal spin-orbit field. The AC current is along y direction and magnetic field is along $\pm y$ direction.

In this SOT study, we relate the second-harmonic resistance to the current-induced spin-orbit field. In practice, there are other possible contributions. For example, when we measure the out-of-plane magnetic hysteresis, there is also nonzero second-harmonic resistance as shown in Figure 2-1b. Here, the second-harmonic resistance has two different contributions: 1) overall symmetric offset resistance ($\sim 0.01\Omega$) due to Seebeck effect and/or asymmetry of voltage probes, 2) asymmetric resistance ($\sim \pm 0.01\Omega$) due to the Anomalous Nernst-Ettingshausen effect (ANE) [14]. These signals are not related to the SOT study, and after careful subtraction following formula, $R^{2\omega} = R_{\text{raw}}^{2\omega} - R_{\text{ANE}} \frac{R^{1\omega}}{R_A} - R_{\text{offset}}$, where $R_{\text{raw}}^{2\omega}$ is the raw data (blue curve in Figure 2-1b), $R_{\text{ANE}} = 0.01\Omega$ and $R_{\text{offset}} = 0.01\Omega$, we could get the real second-harmonic signal related to the spin-orbit torque we will discuss below. Here, after the subtraction, the second-harmonic signal is zero, since tilting angle induced by AC current is given by $\theta(I) = \frac{\Delta H_L \sin \omega t}{H_z + H_k}$ and there is not second-harmonic resistance emerging.

In above, the measured longitudinal spin-orbit field is at $\theta=0^\circ$. We can also measure the current-induced spin-orbit field at $\theta=90^\circ$. To do this, we need to apply large magnetic field to align the magnetization along $\pm y$ direction. Then, when we apply AC current through the film, the current-induced spin-orbit torque is along $\pm z$ direction, since the magnetization is along $\pm y$ direction and $m \times x$ is pointing to $\pm z$ direction (see left top inset of Figure 2-3). So, the tilting angle $\theta(I) = \frac{\pi}{2} - \delta\theta_M \approx \frac{\pi}{2} + \frac{\Delta H_L \sin \omega t}{H_y - K}$, where the K is effective in-plane anisotropy field (describe how large field is required to align the magnetization to in-plane) and $\delta\theta_M$ is a very small angle. So, $R_{\text{AHE}}(t) = R_{\text{AHE}}^{1\omega} - 2R_{\text{AHE}}^{2\omega} \sin(\omega t) = R_A \cos \theta \approx -R_A \frac{\Delta H_L \sin \omega t}{H_y - K}$, and second-harmonic resistance is

$$R_{\text{AHE}}^{2\omega} = \frac{1}{2} \frac{R_A \Delta H_L}{H_y - K} \quad (18)$$

Figure 2-3 shows the second-harmonic resistance curves at different AC current amplitudes, 0.1mA, 0.5mA and 1mA. These curves can be fitted by Eq. 18 very well at large field regime as shown in the left bottom inset of Figure 2-3. From the fitting (two fitting parameters are used, K and ΔH_L), we know that the current-induced longitudinal spin-orbit field is around 0.23Oe at 0.1mA, 1.12Oe at 0.5mA and 2.25Oe at 1mA. This time, the magnitude of ΔH_L is almost proportional to the current amplitude, which indicates that the system is still in the linear regime. The efficiency of current-induced spin-orbit field, $\Delta H_L/J$, is around $3.145 \times 10^{-6} \text{Oe}/(\text{A}/\text{cm}^2)$ below 1mA. We summary the spin-orbit field for both out-of-plane and in-plane in Figure 2-4. The angle dependence of longitudinal spin-orbit field is not well understood at current stage. In addition, the negative sign of longitudinal spin-orbit field means that when current is passed through y direction, the out-of-plane longitudinal spin-orbit field is pointing to $-y$ direction (magnetization is along $+z$ direction), and in-plane longitudinal spin-orbit field is pointing $+z$ direction (magnetization is along $+y$ direction).

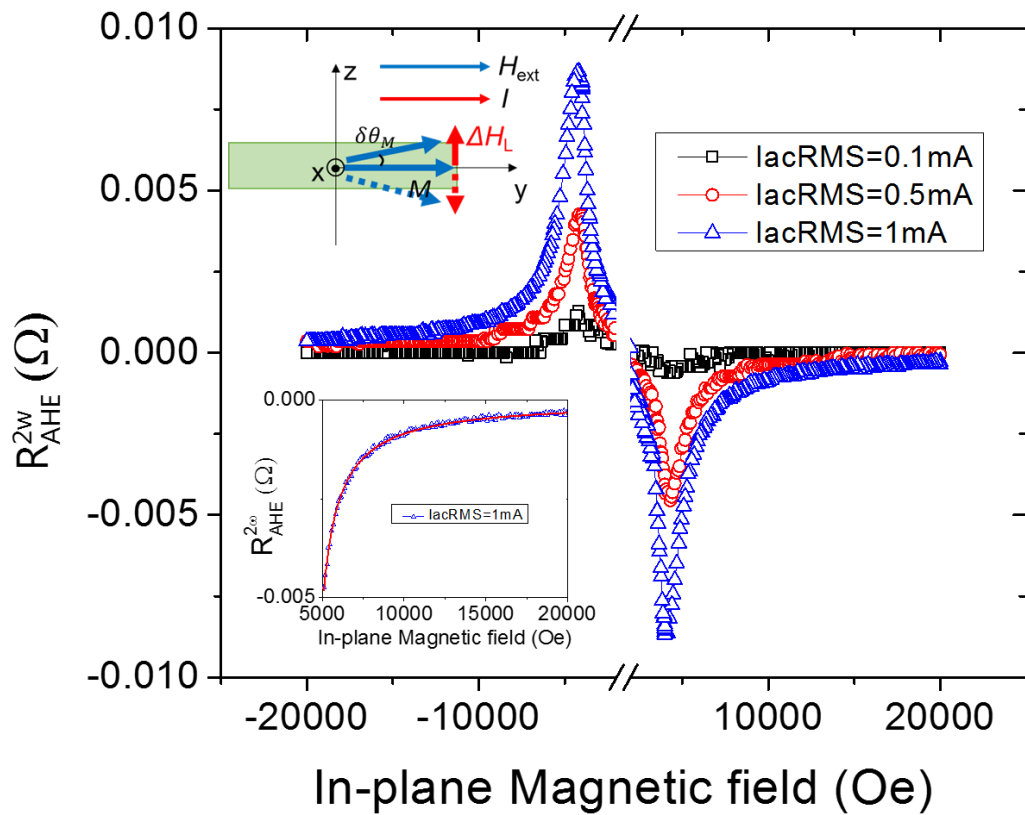


Figure 2-3 Second-harmonic resistance due to the current-induced (in-plane) longitudinal spin-orbit field. Left top inset is an illustration of measurement method. Left bottom inset indicates the goodness of fitting using Eq. 18.

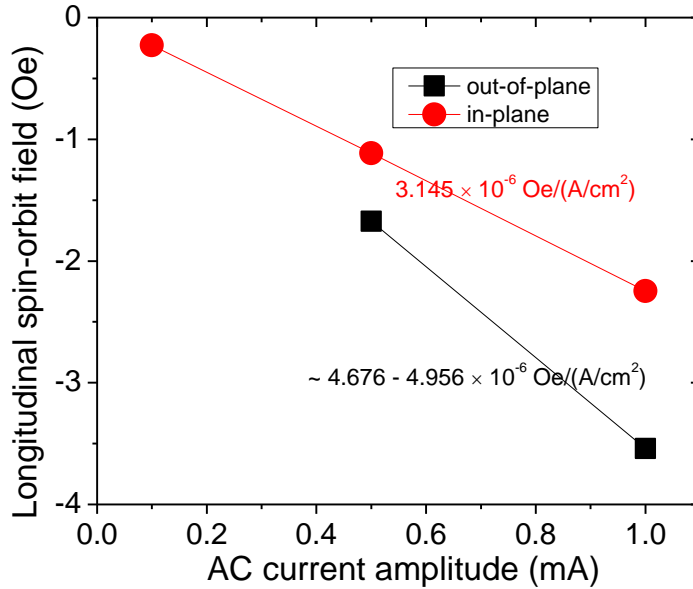


Figure 2-4 summary of current-induced longitudinal spin-orbit fields for both out-of-plane and in-plane magnetizations.

2.1.2 Current-induced magnetization switching

In the previous section, we confirm the existence of current-induced longitudinal spin-orbit field and know that the field is pointing to $-y$ direction when current is applied in $+y$ direction. We expect that if the SOT is strong enough, the magnetization could be switched in the presence of external magnetic field as we discussed in section 1.3.2 and Figure 1-8. Here, we put Figure 1-8c in the Figure 2-5a for your convenience. In the absence of in-plane external magnetic field, the mirror symmetry of Ta/CoFeB/MgO is not broken, and thus current could not give deterministic switching. In the presence of y -direction external magnetic field, the energy barrier for switching from down to up is reduced and correspondingly the energy barrier for switching from up to down is increased. So, magnetization pointing up is the preferred direction. If the current density along $+y$ direction is large enough, we expect that the magnetization could be switched from down to up. If the

external magnetic is along $-y$ direction, magnetization pointing down is the preferred direction, and the switching process is reversed. This is confirmed by experimental data shown in Figure 2-5b. In the presence of $+y$ direction external magnetic field, the positive current ($+y$ direction) will give rise to a positive anomalous Hall resistance (magnetization is up). If the external magnetic field is reversed, the positive current will give rise to a negative anomalous Hall resistance.

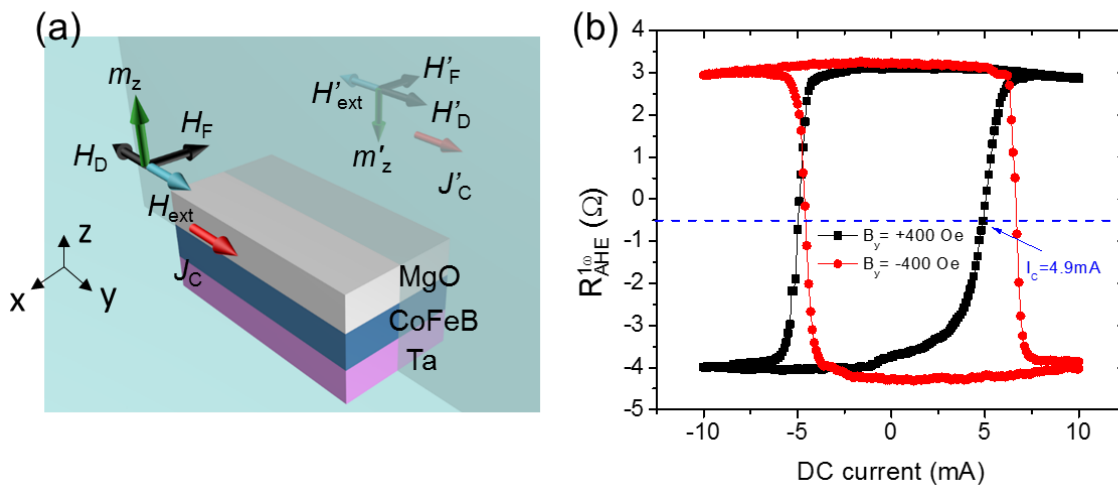


Figure 2-5 Current-induced magnetization switching in Ta/CoFeB/MgO. (a) Principle of current-induced magnetization switching in the presence of external magnetic field. (b) Experimental realization of current-induced switching. At $+y$ direction external magnetic field and $+y$ direction DC current, the magnetization is pointing up (anomalous Hall resistance is positive). The critical switching current is defined as the current value when the corresponding anomalous Hall resistance is zero (there is an overall resistance offset here, and -0.5Ω corresponds to zero anomalous Hall resistance). Here, the critical switching current is around 4.9mA for switching from down to up in the presence of $+y$ direction external magnetic field.

The critical current for switching is defined as the current value when the anomalous Hall resistance is zero. Since there is always a sample-dependent resistance offset, we need to subtract it to get the critical current. If the external magnetic field is 400 Oe along the +y direction, the critical current is 4.9mA to switch the magnetization from down to up (see Figure 2-5b). We plot the magnetization as a function of external magnetic field and DC current in Figure 2-6, which is called switching phase diagram. From the diagram, we can easily see what the magnetization state is given an external magnetic field and an in-plane DC current. Moreover, the switching behavior is clearly not in the single-domain regime (Stoner–Wohlfarth model). Thermal excitation is involved in the switching process.

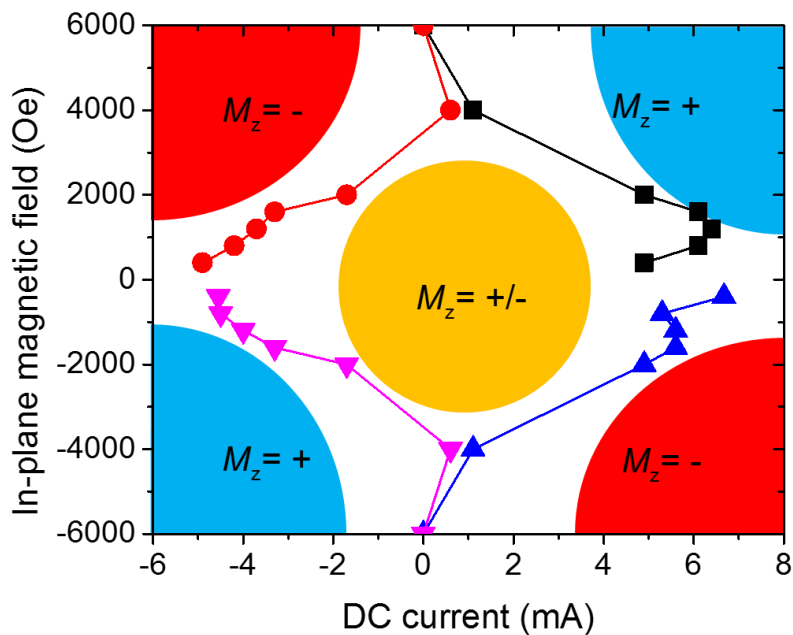


Figure 2-6 Switching phase diagram for Ta/CoFeB/MgO. The center region is indeterministic, and the magnetization can be either pointing up or down. At the right top corner, where both DC current and external magnetic field are along +y direction, magnetization is deterministically pointing up.

In our Ta/CoFeB/MgO devices, the critical switching current density is at the level of 10^6 A/cm², which is comparable with the critical current density for STT-MRAMs [23]. We should notice that the thickness of Ta we use is 6nm. If we could further reduce the thickness of Ta and thus increase

$\frac{A_{\text{Ta}}(\text{cross-section})}{A_{\text{CoFeB}}(\text{top-view area})}$, the switching current could be reduced according to Eq. 14.

2.2 SOT in TI/Cr-TI bilayer and Cr-TI single layer

2.2.1 Motivation for studying SOT in TIs

In this section, we study the SOT in TIs, especially in Cr-(BiSb)₂Te₃/(BiSb)₂Te₃ heterostructure and Cr-(BiSb)₂Te₃ single layer, using the same technique as above. Bi₂Se₃, Bi₂Te₃, and Sb₂Te₃ are three-dimensional (3D) topological insulators, in contrast to the two-dimensional (2D) topological insulators, HgTe quantum wells [26-28]. For 2D TIs, they have two edge channels with spin-polarized carriers. For 3D TIs, they are semiconductors with inverted band gap and nontrivial band topology (the topological Chern number is nonzero). The main reason that make them have inverted band gap is the strong spin-orbit coupling in these materials. At the interface between nontrivial TIs and trivial insulators (e.g., vacuum, oxide), there are metallic surface states with zero band gap and linear energy dispersion (see Figure 2-7a). Good introduction and review materials of TIs can be found in Refs. [29, 30]. At the surface of 3D TIs, the carriers are spin-polarized as shown in Figure 2-7, and we call them surface state carriers. When electrons have positive momentum k_x , their spin direction will point to $-y$ direction; when electrons have negative momentum $-k_x$, their spin direction will point to $+y$ direction. This phenomenon is called spin-momentum locking. This feature could be electrically probed using ferromagnetic contacts and the magnetoresistance effect. However, typical 3D TIs, such as Bi₂Se₃, Bi₂Te₃, and Sb₂Te₃, have a lot of (n-type) bulk carriers due to intrinsic growth defect and the Fermi level is hard to be tuned

into the bulk band gap. These bulk carriers are not spin-polarized, and thus give rise to a huge background signal that make the hysteresis signal hard to detect.

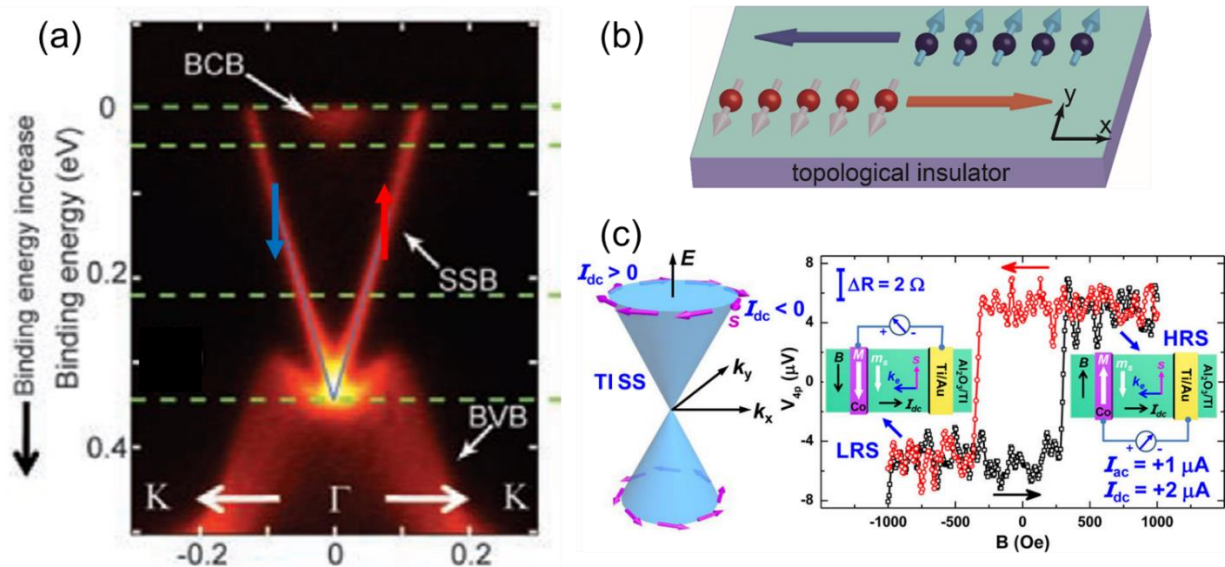


Figure 2-7 Spin-momentum locking for surface state carriers in topological insulators. (a) Angle-resolved photoemission spectrum (ARPES) of intrinsic 3D Bi_2Te_3 . Intrinsic Bi_2Te_3 is n-type due to growth defect. The Fermi level is in the bulk conduction band (BCB). Between BCB and bulk valence band (BVB), there are two surface state bands (SSBs) with linear energy dispersion. In addition, the carriers in SSBs are spin-polarized: electrons at SSB with positive crystal momentum are spin-up polarized, and electrons at SSB with negative crystal momentum are spin-down polarized. (b) Spin-momentum locking on the surface of TIs. When electrons are moving with a positive k_x , their spins are pointing to $-y$ direction; when electrons are moving with a negative k_x , their spins are pointing to $+y$ direction. (c) Left panel: 3D illustration of spin-polarized surface state carriers. Electrons at the upper cone has a spin locked to momentum in a clockwise fashion, and electrons at the lower cone has a spin locked momentum in an anticlockwise fashion. Right panel: experimental demonstration of spin-momentum locking in $(\text{BiSb})_2\text{Te}_3$. Note that magnetic moment direction of electron is opposite to the spin direction due to the negative charge. Details are given

in the main text. (a) is from [31], reprinted with permission from AAAS. (c) is reprinted with permission from [32], Copyright 2014 American Chemical Society.

$(\text{BiSb})_2\text{Te}_3$ is a 3D ternary topological insulator with very low bulk conduction at low temperature. With electrostatic gating and careful composition tuning, there is an ambipolar effect observed in $(\text{BiSb})_2\text{Te}_3$ [33], which indicates that Fermi level is close to the center of bulk band gap. Jianshi Tang et al. [32] successfully detected the spin-polarized surface state carriers in $(\text{BiSb})_2\text{Te}_3$. They used Co as the ferromagnetic contacts. Constant DC current along +x direction is applied and thus electrons have a spin direction pointing to +y direction. The external magnetic field is applied along $\pm y$ direction to switch the magnetization of ferromagnetic contact Co. The voltage signal used to detect the spin polarization is between the Co and normal contact Ti/Au. If the surface state electrons are not spin-polarized, we do not expect see any hysteresis. Indeed, they observed the hysteresis: when the magnetization of Co is pointing to + y direction, there is a high resistance signal (antiparallel state between magnetic moment of surface state carriers and magnetization of Co contact); when the magnetization of Co is pointing to -y direction, there is a low resistance signal. This confirms that surface state electrons are spin-polarized and it follows the rule of spin-momentum locking. Note that this experiment was conducted at cryogenic temperature. Recently, there are several works that indicate the existence of spin-momentum locking at room temperature [34, 35].

The spin-momentum locking can be viewed as an extreme case of SHE: as long as the electron momentum direction is fixed, the spin direction will also be fixed to a specific direction. TIs are a class of materials that have this feature and this motivates us to study SOTs in TIs. There is also a theoretical proposal about the giant SOT in TI/ferromagnet heterostructure [36]. In the next section, we will show that there is a giant SOT in Cr-doped TI/TI heterostructure, where Cr-doped TI is the ferromagnetic layer with perpendicular magnetic anisotropy.

2.2.2 Experimental demonstration of giant SOTs in Cr-TI/TI bilayer

Experimental demonstration of giant SOTs is initially done by my colleagues, Yabin Fan et al. [37], using Cr-(BiSb)₂Te₃(6)/(BiSb)₂Te₃(3) bilayer. In this section and next section, I use a similar sample, Cr-(BiSb)₂Te₃(3)/ BiSb)₂Te₃(9) bilayer with different thickness, to extract the SOT as an exercise. Width of Hall bar channel is 10um. More experiments on TIs in next chapter are based on these two sections. Unless specifically stated otherwise, all measurements in this thesis related to Cr-TIs are done at 1.9K, because magnetic TIs have a fairly low Curie temperature (around 10 – 30K depending on the doping level). Figure 2-8a gives the film details and for the growth information, you may want to read Ref. [37]. The out-of-plane magnetic hysteresis is shown in Figure 2-8b, which indicates that Cr-(BiSb)₂Te₃ has an out-of-plane magnetic anisotropy. The coercivity field is around 100 Oe and the AHE coefficient depends on the current amplitude. In addition, there is a large ordinary Hall resistance in the hysteresis curves. From the linear regime at large magnetic field, we could extract the sheet carrier density. Figure 2-8c summarizes the current dependence of AHE coefficient and sheet carrier density.

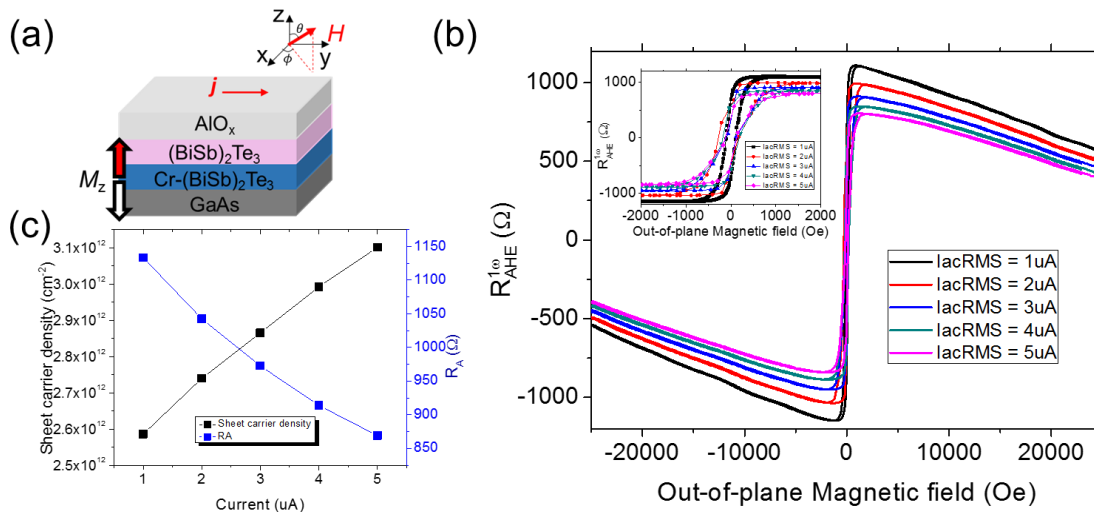


Figure 2-8 Schematic and basic properties of Cr-TI/TI bilayer. (a) Schematic of the Cr-TI/TI bilayer. The substrate is GaAs and top AlO_x is the capping layer used to protect TI film from oxidation and other potential air molecule-induced degradations. (b) Out-of-plane magnetic hysteresis of Cr-TI/TI bilayer. Here, large ordinary Hall resistance is observed at large field and it is current amplitude-dependent. The coercivity field is around 100 Oe, and $R_A \approx 1 \text{ k}\Omega$ depending on the current magnitude. (c) Current-dependent sheet carrier density and AHE coefficient.

Since $(\text{BiSb})_2\text{Te}_3$ has very strong spin-orbit coupling and it has surface state carriers that are spin-momentum locked (spin-polarized), we expect that by passing through the Cr- $(\text{BiSb})_2\text{Te}_3$ / $(\text{BiSb})_2\text{Te}_3$ bilayer, a large longitudinal spin-orbit field (damping-like field) can be induced. Here, we measure the in-plane longitudinal spin-orbit field as we did for Ta/CoFeB/MgO. Eq. 18 is used to extract the current-induced longitudinal spin-orbit field. Different from previous Ta/CoFeB/MgO case, we independently extract the K (or H_k) using polar angle θ of large external magnetic field dependent first-harmonic anomalous Hall resistance. The equilibrium position of magnetization is determined by the out-of-plane anisotropy field and the external magnetic field. The tangent components of these two fields with respect to the magnetization are illustrated in Figure 2-9a, and they give rise to the equation that determines the equilibrium of magnetization:

$$H_k \sin \theta_M \cos \theta_M = H_{ext} \sin(\theta_B - \theta_M) \quad (19)$$

where we assume the external magnetic field is large to make the angle $\theta_B - \theta_M$ small. The angle-dependent first-harmonic Hall resistance is shown as dashed curves in Figure 2-9b, which has weird shape due to the large ordinary Hall resistance background at 3 Tesla external magnetic field. After the subtraction of ordinary Hall resistance, the angle-dependent first-harmonic anomalous Hall resistance is shown as solid curves in Figure 2-9b. By fitting the curves using Eq. 19, we could obtain the anisotropy field K as a function of current amplitude (see Figure 2-9b). As

the current amplitude increases, the anisotropy field decreases, which is reasonable and may be due to the current-induced Joule heating.

After obtaining information about R_A and K , we are in a position to extract ΔH_L using Eq. 18. The second-harmonic resistance under in-plane magnetic field is shown in Figure 2-10a. The second-harmonic resistance is not near zero even at very large magnetic field, which indicates a very large longitudinal spin-orbit field generated by injection current. Figure 2-10b gives the extracted values of longitudinal spin-orbit field, which is extraordinarily large compared with the case of Ta/CoFeB/MgO. The ratio of spin-orbit field over current density ($\Delta H_L/J$), or so called efficiency of current-induced spin-orbit field, is nearly five orders of magnitude larger than the case in Ta/CoFeB/MgO. In Ref. [37], the reported ratio ($\Delta H_L/J$) was around three orders of magnitude larger than those reported in heavy metal/ferromagnet heterostructures [14, 24].

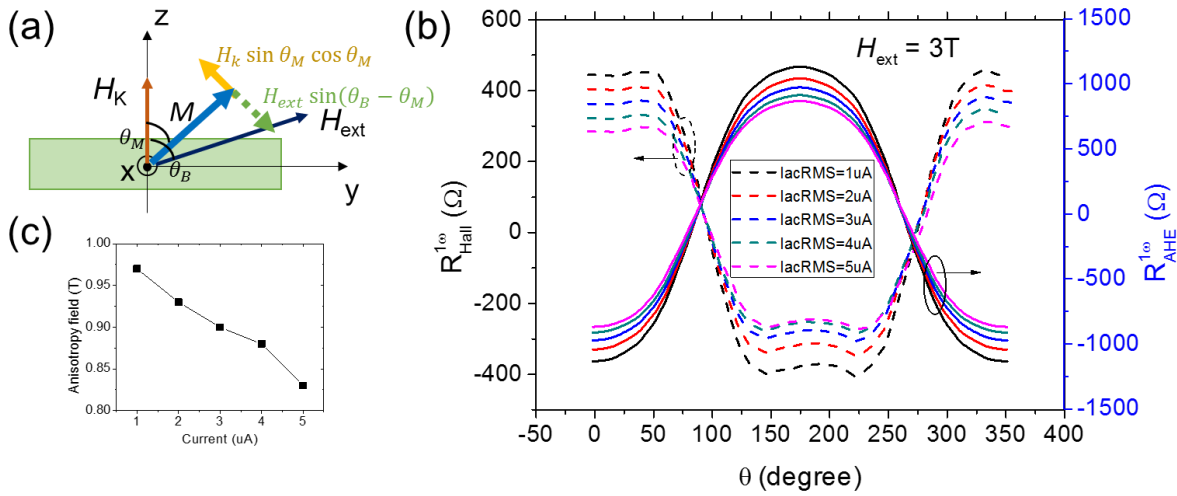


Figure 2-9 First-harmonic resistance as a function of external magnetic field polar angle θ in yz plane. (a) Equilibrium position of magnetization is determined by the effective out-of-plane anisotropy field and large external magnetic field using Eq. 19. (b) First-harmonic resistance (raw data, including ordinary Hall resistance, dashed curves) and first-harmonic anomalous Hall

resistance (after subtraction of ordinary Hall resistance, solid curves) as a function of external magnetic field polar angle θ . By fitting the solid curves with Eq. 19, current-dependent effective out-of-plane anisotropy field could be obtained and it will be used to fit (in-plane) longitudinal spin-orbit field using Eq. 18. (c) Extracted anisotropy field as a function of current amplitude.

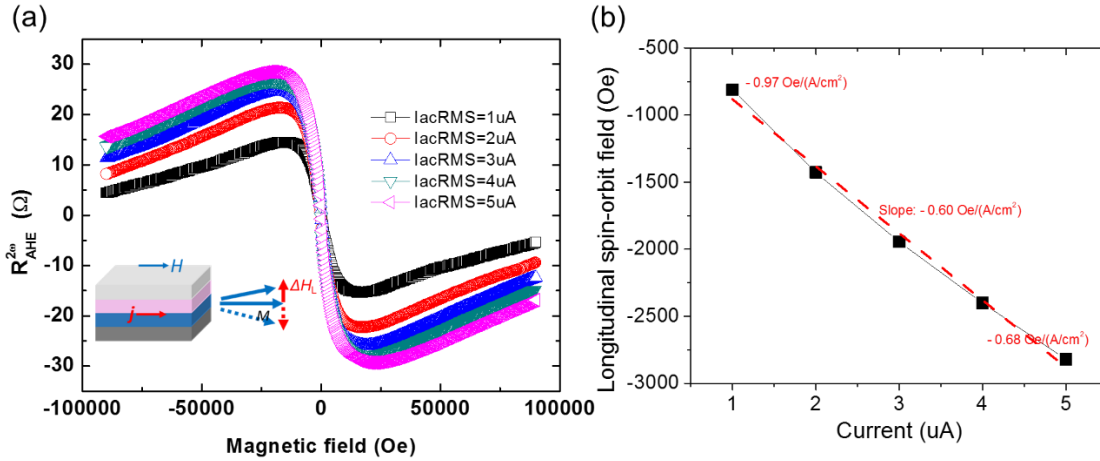


Figure 2-10 Second-harmonic resistance and current-induced longitudinal spin-orbit field for the Cr-Tl/Tl bilayer in the presence of large in-plane magnetic field. (a) Second-harmonic resistance as a function of external magnetic field. Left bottom inset is the illustration of measurement principle. (b) Summary of current-induced longitudinal spin-orbit field and corresponding efficiency as a function of current amplitude.

To obtain spin torque ratio ϑ_{SOT} as defined in Eq. 15, we should also take the saturation magnetization into account, $\vartheta_{\text{SOT}} \propto M_s \Delta H_L / J$. Since Cr-(BiSb)₂Te₃ is a dilute doped magnetic semiconductor, it has very low saturation magnetic moments ($\sim 10 \text{ emu}/\text{cm}^3$). For MgO/CoFeB with perpendicular magnetic anisotropy, it has saturation magnetization around one thousands of emu/cm^3 . So, the spin torque ratio of TIs is around three orders of magnitude larger than that of

heavy metals. (In Ref. [37], the reported spin torque ratio is $\sim 140 - 425$, depending on polar angle θ_B of magnetization.)

One important assumption we used to extract the current-induced longitudinal spin-orbit field is that Hall resistance of the Cr-TI/TI bilayer only includes anomalous Hall resistance and ordinary Hall resistance. In reality, planar Hall resistance also involves in the second-harmonic resistance if the transverse (field-like) spin-orbit field is nonzero. Nevertheless, the contribution from PHE is typically one order of magnitude smaller than that from AHE in our Cr-(BiSb)₂Te₃ system, as shown in Ref. [37]. When we consider the contribution from PHE, the extracted spin torque ratio remains almost the same (within 2% difference) [37]. So, our assumption is appropriate here.

According to theoretical study, there are two types of SOT sources beyond SHE potentially existing in TIs: Rashba spin-splitting induced SOTs and surface states induced SOTs [36]. Spin-polarized surface states are extensively studied in 3D TIs. The giant Rashba spin-splitting was also resolved in Bi₂Se₃ using spin-resolved ARPES [38, 39] (see Figure 2-11a). The reason for this giant Rashba spin-splitting is surface band bending. When Bi₂Se₃ is exposed to the air, even in high vacuum (still there are few gas molecules), surface will absorb n-type dopants and make the surface Fermi level buried in bulk conduction band. In the presence of electric field and strong spin-orbit coupling, Bi₂Se₃ develops the bulk subbands with giant Rashba spin-splitting. These two mechanisms give rise to SOTs in opposite direction since electrons in these two bands are spin-polarized in the opposite direction under the electric field [36, 40] (see Figure 2-11b). Nevertheless, these two kinds of SOTs are both based on interfacial effects, and in the next section, we will show interfacial effects dominate and SHE is not the main source for this giant SOT in TIs.

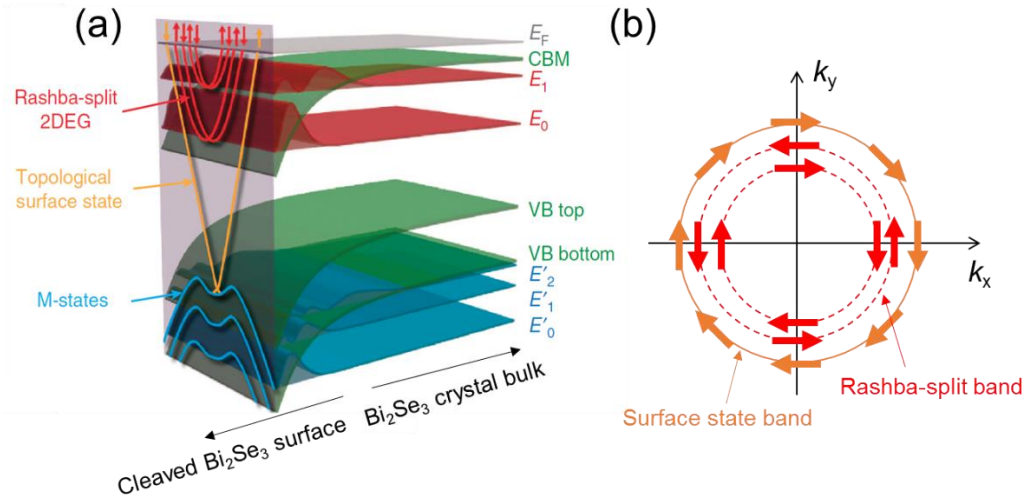


Figure 2-11 Schematic of surface state and Rashba-split two dimensional electron gas (2DEG) at the surface of Bi_2Se_3 . (a) In the direction perpendicular to the film surface, there is a potential gradient (electric field). This electric field leads quantum well states and combined with strong spin-orbit coupling, Rashba-split 2DEG emerges at the surface. In the same time, topological surface state remains uncontested. The Fermi level is in the bulk conduction band. (b) Top view of spin-polarized surface state band and Rashba-split bands. (a) is reprinted by permission from Macmillan Publishers Ltd: Nature Communications [41], copyright 2012.

2.2.3 SOTs in uniform Cr-TI single layer

In this section, we study $\text{GaAs}/\text{Cr}-(\text{BiSb})_2\text{Te}_3(7)/\text{AlO}_x$, where $\text{Cr}-(\text{BiSb})_2\text{Te}_3$ is $(\text{BiSb})_2\text{Te}_3$ uniformly doped by Cr, and it is sandwiched by GaAs and AlO_x , two different dielectric environments (see Figure 2-12a). Main results are obtained by my colleague, Yabin Fan, who provides me research guidance through the first two years of my PhD life. I am involved in the measurement and help him do part of analysis and experiments. Clear out-of-plane magnetic anisotropy is observed in Figure 2-12b, which indicates that $\text{Cr}-(\text{BiSb})_2\text{Te}_3$ has out-of-plane magnetic anisotropy.

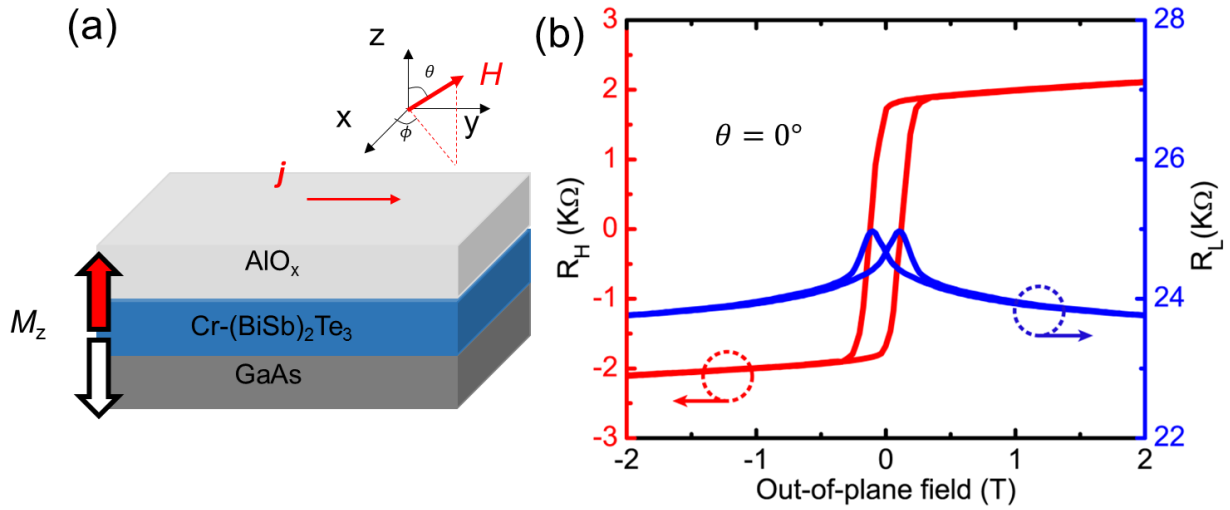


Figure 2-12 Schematic and out-of-plane magnetic hysteresis of GaAs/Cr-(BiSb)₂Te₃/AlO_x. (a) Current is applied along $\pm y$ direction. Cr-(BiSb)₂Te₃ has a perpendicular magnetic anisotropy and is sandwiched with different dielectrics, AlO_x and GaAs. (b) Out-of-plane magnetic hysteresis of for Cr-(BiSb)₂Te₃. R_H is Hall resistance and R_L is (longitudinal) magnetoresistance. Here, Cr-(BiSb)₂Te₃ is p-type and $R_A \approx 1.8\text{k}\Omega$. (b) is provided by Yabin Fan *et al.*

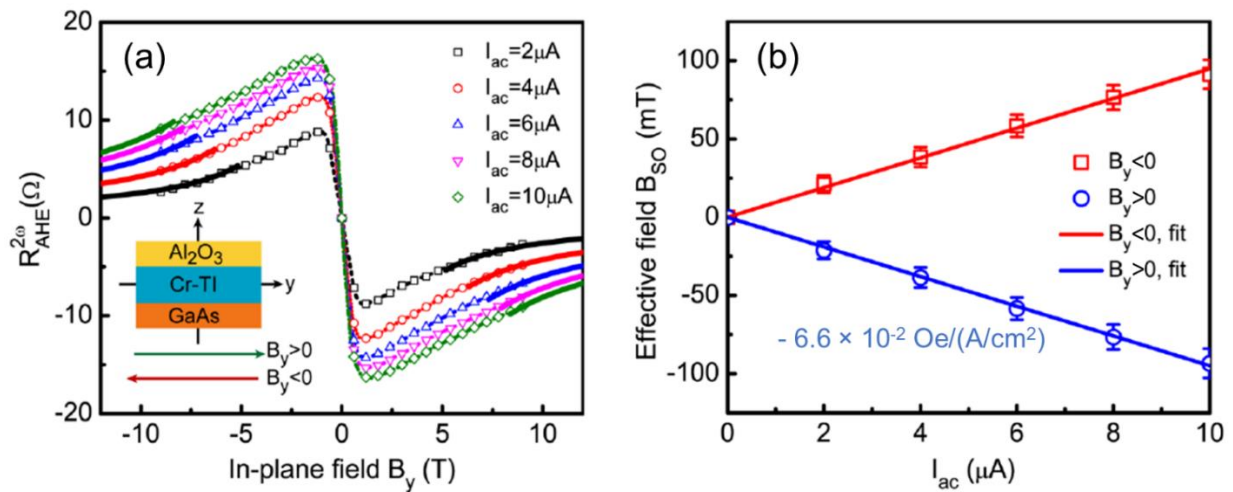


Figure 2-13 In-plane SOT measurement for GaAs/Cr-(BiSb)₂Te₃/AlO_x. (a) Second-harmonic anomalous Hall resistance as a function of in-plane magnetic field. (b) Effective (longitudinal) spin-orbit field as a function of current amplitude. (a) and (b) are provided by Yabin Fan *et al.*

Following the same technique, we extract the SOT as a function of current amplitude from the in-plane second-harmonic measurement (see Figure 2-13). The efficiency, ratio of spin-orbit field over current density, $\Delta H_L/J$, is around one order of magnitude smaller than that in bilayer, but is still three orders of magnitude larger than that in Ta/CoFeB/MgO. Such a huge SOT in uniformly Cr-doped TI films cannot be explained by bulk SHE, since Cr-(BiSb)₂Te₃ itself is symmetric in the z direction. However, the top and bottom interfaces are different, AlO_x/Cr-TI and Cr-TI/GaAs here, and this vertical asymmetry gives rise to a large SOT.

Note that our experiments are conducted at very low temperature (1.9K), since the Cr-TI has a fairly low Curie temperature. We need to emphasize that TI could produce large SOT at room temperature (not confirmed by ourselves yet), and our measurements are only limited by the low Curie temperature of ferromagnetic layer. As reported by Ref. [40], the spin torque ratio of Bi₂Se₃ is measured to be around 2 -3.5 in Bi₂Se₃ /Permalloy (NiFe) heterostructure using spin torque – ferromagnetic resonance (ST-FMR) technique at room temperature, which is still one order of magnitude larger than any other materials. For their measurement, the current is mostly passing through NiFe layer, since NiFe has a much larger conductivity compared with semiconductor Bi₂Se₃. In addition, Bi₂Se₃ has a significant bulk conduction contribution. Therefore, the measured spin torque ratio is not so accurate. Nevertheless, the large spin torque ratio still indicates that SOTs are still very large in TIs. In our experiments, TI and Cr-TI have comparable conductivities, and there is no conductance mismatch issue. For the next step, we are trying to find a room temperature ferromagnet with high resistance and measure the spin torque ratio more convincingly at room temperature. Before that, Cr-TI/TI heterostructure is still a very good platform for studying the origin of this giant SOT.

2.3 Current-induced magnetization switching in magnetic TIs

In the previous section, giant SOTs are demonstrated in both Cr-TI/TI bilayer and Cr-TI single layer. We expect that by passing current through the patterned Hall bar devices, the magnetization can be switched following the same mechanism in Ta/CoFeB/MgO case.

Figure 2-14a gives the experimental results of TI/Cr-TI bilayer. When the injection current and external magnetic field are both along +y direction, a positive anomalous Hall resistance is obtained, which indicates that the magnetization is pointing towards up. Notice that the first-harmonic resistance is around 50Ω , much smaller than R_A of this device ($\sim 1\text{k}\Omega$, see Figure 2-8b), which says that the magnetization is tilted slightly up, instead of pointing up (+z direction). The current-induced longitudinal spin-orbit field in Cr-TI/TI/ AlO_x has the same direction with Ta/CoFeB/MgO, and thus TIs have an opposite effective spin Hall sign compared with Ta considering the fact that the position of ferromagnetic layer is opposite [37]. TIs have the same spin Hall sign with Pt in this perspective, and it is confirmed by ST-FMR measurement at room temperature [40]. However, as we argued above, SHE is not a dominant effect in terms of generating SOTs in TIs. So, this effective spin Hall sign has limited meaning and may only provide guidance in predicting the switching direction. In addition, the critical current for switching is almost zero ($\sim 0.1\mu\text{A}$), since the SOT of TI is giant and external magnetic field is also quite large compared with the field used in Ta/CoFeB/MgO.

Figure 2-14b gives the experimental results of current-induced magnetization switching in Cr-TI single layer. The switching direction is the same as the case of Cr-TI/TI bilayer. However, since the Cr-TI is uniformly Cr-doped, there is no meaning to say the sign of spin Hall angle. We need to clarify which interface contributes more SOTs.

In the next chapter, we first propose a simple model to explain interface, particularly the surface states, dominated SOTs and switching behaviors in section 3.1. Then, we design two experiments to verify and further understand the model in section 3.2 and 3.3.

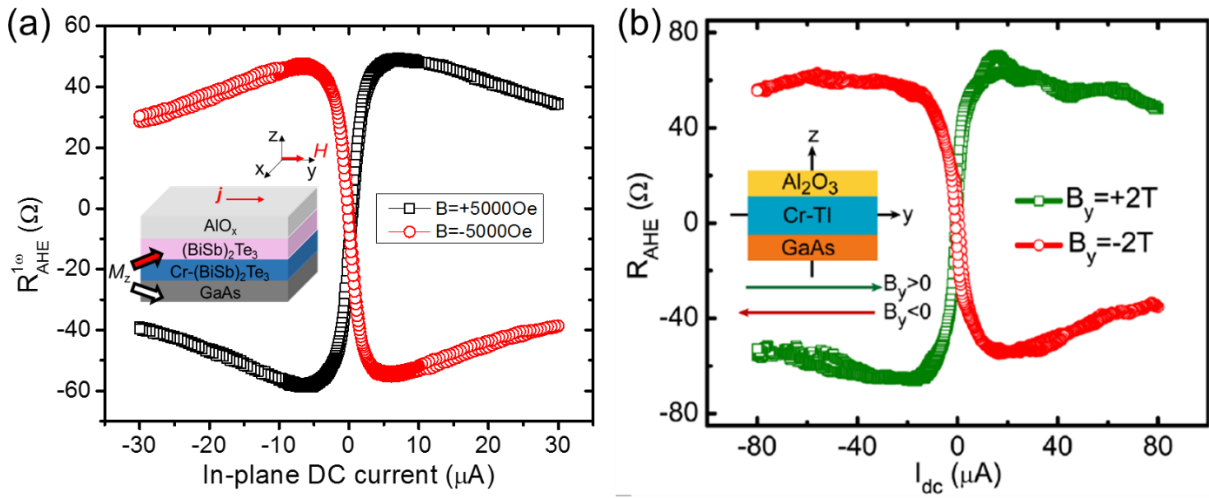


Figure 2-14 Current-induced magnetization switching in the Cr-TI/TI bilayer and the Cr-TI single layer. (a) Current-induced magnetization switching in the Cr-TI/TI bilayer. If the injection current and external magnetic field are both along +y direction, the magnetization will point towards up (not perpendicularly up, tilted). If the injection current is along -y direction and external magnetic field is along +y direction, the magnetization will point towards down (not perpendicularly down, tilted). (b) current-induced magnetization switching in the Cr-TI single layer. (b) is provided by Yabin Fan *et al.*

Chapter 3. Evidences for surface state spin-orbit torque in TIs

In the previous chapter, we demonstrate that topological insulators have giant spin torque ratio. In other words, by passing current through TIs, giant SOTs can be generated to efficiently manipulate the magnetization of magnetic TIs. In this chapter, main effort will be put in understanding the origin of this giant SOT. First, we propose a model for surface state induced magnetization switching in section 3.1. Then, we use two experiments in section 3.2 and 3.3 to verify the model and thus show the strong evidence of surface state dominated SOTs in TI-based systems.

3.1 Model for surface state induced SOTs

As discussed in section 1.3.2, SHE is the main mechanism for current-induced magnetization switching in heavy metal/ferromagnet heterostructures, such as Pt/Co/MgO and Ta/CoFeB/MgO [20, 21]. Under the in-plane electric field, electrons are deflected vertically and depending on the deflection direction (see Figure 3-1a), we can define the sign of spin torque ratio, ϑ_{ST} . As we defined in section 2.1.1, +y direction is the positive direction for both injection current and current-induced longitudinal spin-orbit field. The longitudinal (damping-like) spin-orbit field is given by $\Delta\mathbf{H}_L = \vartheta_{ST}\mathbf{M} \times \mathbf{z} \times \mathbf{J}$ [14], and thus negative sign of ϑ_{ST} gives rise to a positive spin-orbit field for the deflected up current (see Figure 3-1b). For the deflected down current, the spin-orbit field is given by $\Delta\mathbf{H}_L = -\vartheta_{ST}\mathbf{M} \times \mathbf{z} \times \mathbf{J}$, and thus negative sign of ϑ_{ST} gives rise to a negative spin-orbit field. Using this convention, we can find the sign of spin torque for Ta and Pt. From section 2.1.1, we know that current deflection direction is up for Ta/CoFeB/MgO heterostructure and a positive current gives rise to a negative longitudinal spin-orbit field. So, the sign of spin torque ratio for Ta, ϑ_{Ta} , is positive. In Refs. [20, 21, 25], we know that current-induced magnetization switching direction is opposite for Ta and Pt, and thus $\vartheta_{Pt} < 0$.

SHE is a bulk effect, whereas Rashba effect can be either bulk or interfacial depending on the material. Bulk Rashba-splitting induced magnetization switching between two in-plane easy axes was demonstrated in diluted magnetic semiconductor, such as (Ga,Mn)As with zinc-blende crystal structure [16]. Interfacial Rashba effect may also generate large SOT and cause magnetization switching according to recent SOT study experiments in Ta/CoFeB/TaO_x and Pt/CoFeB/MgO by oxygen manipulation [19, 22]. In addition to Rashba effect and SHE, topological surface states could also give rise to SOTs in TI-based magnetic systems. As we discussed in section 2.2.3, current-induced giant SOTs in uniformly Cr-doped TIs cannot originate from bulk SHE or bulk Rashba effect, since Cr-TI itself is symmetric along the z direction.

In TIs, Rashba spin-split 2DEG and surface state electrons give opposite spin torques, and Rashba spin-split 2DEG density is smaller compared with the density of surface state electrons at interface [40]. In addition, there is no evidence showing that both top and bottom surface of TIs have Rashba spin-split 2DEG. So, if only top surface of TI-based magnetic systems has Rashba spin-split 2DEG, it is unreasonable to see current-induced switching in Cr-TI/TI bilayer as shown in section 2.3, since top surface is far away from the magnetic layer (~9nm). Based on these facts, we propose a model based on surface state-induced magnetization below.

When current is passed through TIs, electrons are deflected vertically. Typically, when we talk about the chirality of Dirac surface state fermion, top view of spin-polarized surface state band is used as shown in Figure 3-1c. For the point of interaction between electrons and magnetic moments, the deflection direction is also critical. Figure 3-1c is suitable for electrons deflected down to the bottom surface state. However, for electrons deflected up to the top surface, bottom view of spin-polarized surface state should be used, and it shows opposite chirality from electrons deflected down (see Figure 3-1d). Therefore, when current is applied through TIs, opposite SOTs are generated from top and bottom surface states. However, since the TI-based magnetic structure cannot be perfectly symmetrically at the vertical (z) direction, there may be a net SOT

generated by passing an in-plane current. As we all know from section 2.2.3, giant SOTs are generated by injection current in the Cr-TI single layer, and this is a strong evidence of non-equal surface state induced SOTs in TI-based magnetic systems. In the following, we are going to analyze the origin of SOT and the sign of spin torque ratio in TIs using a simple model.

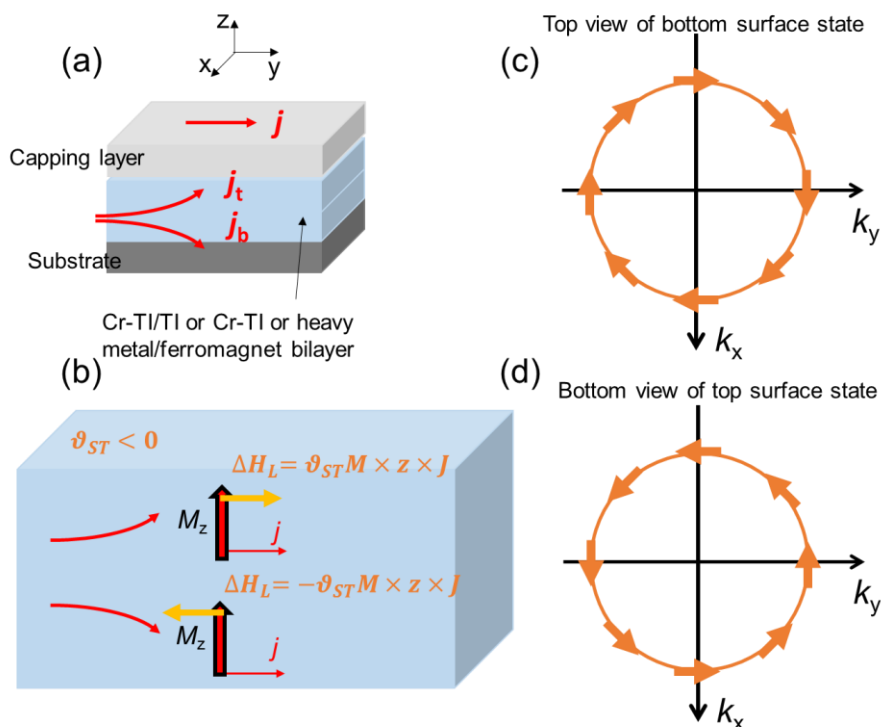


Figure 3-1 General definition for the sign of spin torque ratio and current-induced spin polarization at top and bottom surface in TI-based magnetic heterostructures. (a) Electron deflection under the electric field in magnetic heterostructures. (b) For the deflected up current, the fact that a positive current induces a positive longitudinal spin-orbit field indicates that the sign of spin torque ratio is negative. For the deflected down current, a positive current in materials with negative spin torque ratio sign would give a negative longitudinal spin-orbit field. (c) Spin of electrons deflected to bottom surface is locked to the momentum in a clockwise fashion from top view (magnetic moments are above the bottom surface states). (d) Spin of electrons deflected to bottom surface

is locked to the momentum in an anticlockwise fashion from bottom view (magnetic moments are below the bottom surface states).

In the Cr-(BiSb)₂Te₃/(BiSb)₂Te₃ bilayer, the current-induced magnetization switching has the same direction as that in Ta/CoFeB/MgO. However, bottom surface state electrons contribute to the longitudinal (damping-like) spin-orbit field in Cr-TI/TI bilayer, since the top surface is far away from the magnetic layer (~9nm, see Figure 3-2a-b). Effectively, we can think that electrons deflected down give rise to the SOT. Therefore, $\vartheta_{BSS} > 0$ for bottom surface state electrons considering that Cr-TI/TI and Ta/CoFeB/MgO have the opposite stack order and the same switching direction. When current is applied along $-y$ direction, electrons have $+y$ direction momentum. According to spin-momentum locking of bottom surface (top view of bottom surface state band), electrons have $+x$ direction spin polarization and $-x$ direction magnetic moment. The current-induced longitudinal spin-orbit field can be written as $\Delta H_{LB} = \vartheta_{BSS} M \times z \times j_b$, where j_b is the current deflected to the bottom. Since the top surface contributes zero spin-orbit field, the total spin-orbit field is ΔH_{LB} , along $+y$ direction. In the presence of $+y$ direction, current along $-y$ direction is energetically in favor of magnetization pointing down, and thus injection current along $-y$ direction will induce magnetization switching (see Figure 3-2b). If the current is applied along $+y$ direction, bottom surface state electrons generate opposite spin-orbit field that is along $-y$ direction, and it leads to no switching since the initial magnetization is already pointing up (see Figure 3-2c-d).

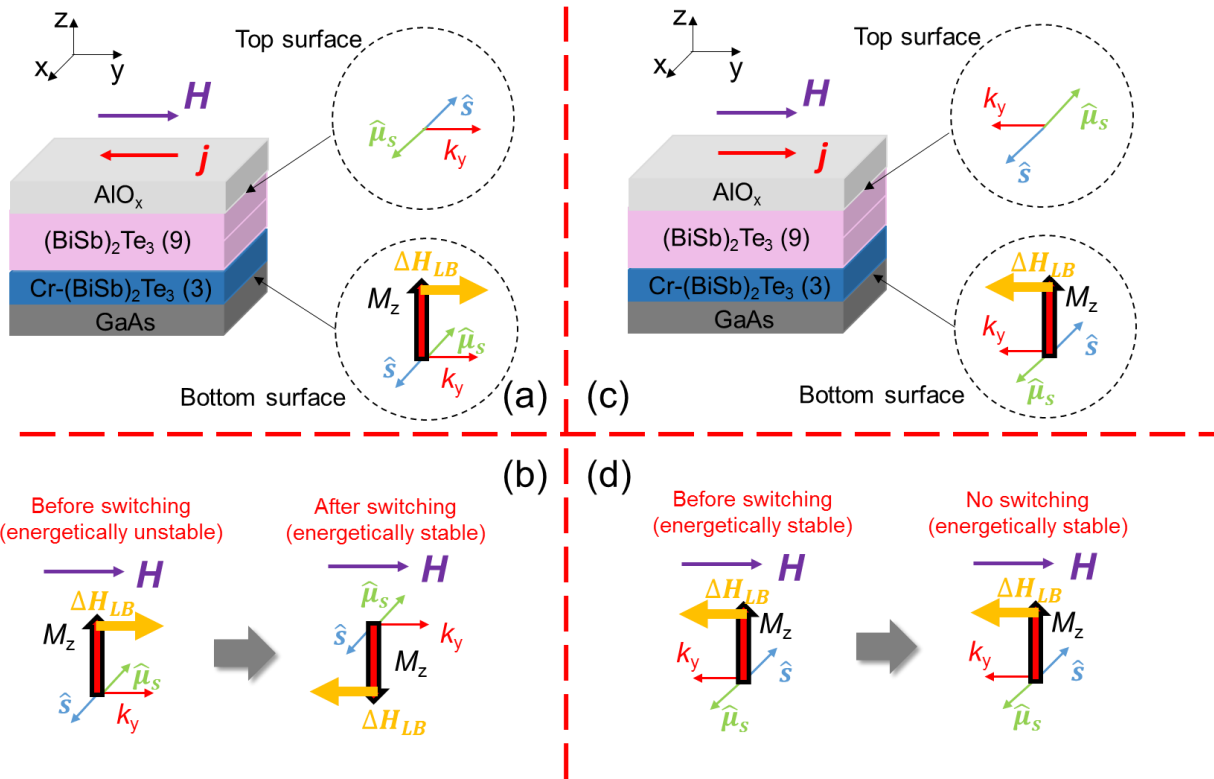


Figure 3-2 Model for topological surface state induced (longitudinal) damping-like spin-orbit field and magnetization switching in the Cr-TI/TI bilayer. (a) Longitudinal spin-orbit field generated by top and bottom surface state with initial magnetization along +z direction. Current is applied along $-y$ direction and thus electron momentum is along $+y$ direction. Since top surface is far away from magnetic moments, there is no spin-orbit field ($\Delta H_{LT} = 0$). Bottom surface state induced longitudinal spin-orbit field, ΔH_{LB} , is pointing to $-M_z \times z \times J$. \hat{s} is the electron spin direction and $\hat{\mu}_s$ is electron magnetic moment (electron has negative charge). (b) Both surface states induced total longitudinal spin-orbit field in the Cr-TI/TI bilayer is given by $\Delta H_L = \Delta H_{LB} - \Delta H_{LT} = \Delta H_{LB}$. ΔH_L is pointing to $+y$ direction. This spin-orbit field leads magnetization switching in the presence of $+y$ direction external magnetic field. (c) Longitudinal spin-orbit field generated by top and bottom surface state with initial magnetization along $+z$ direction when current is applied along $+y$

direction. The direction of spin-orbit field is opposite with the case in (a). (d) No switching since initial state is energetically preferred in the presence of +y direction external magnetic field.

In the Cr-(BiSb)₂Te₃ single layer, both top and bottom surface state electrons contribute to the SOT. When current is applied along -y direction, the spin-orbit field generated by bottom surface state electrons is still $\Delta H_{LB} = \vartheta_{BSS} M \times z \times j_b$ that is along +y direction (see Figure 3-3a). Since top surface state electrons are equivalent to electrons deflected to the top, they must generate opposite spin-orbit field compared with bottom surface state electrons. This is manifested by the opposite chirality looking from the top and bottom as shown in Figure 3-1c-d. Therefore, the total longitudinal spin-orbit field is given by $\Delta H_L = \Delta H_{LB} - \Delta H_{LT} = \vartheta_{BSS} M \times z \times j_b - \vartheta_{TSS} M \times z \times j_t$, where ϑ_{BSS} and ϑ_{TSS} are both positive and the negative sign before ϑ_{TSS} indicates that anticlockwise chirality (bottom view of surface state band) is used. j_b and j_t are the current deflected to the bottom and top, respectively. From section 2.2.3, we know that the Cr-TI single layer has the same switching direction as the Cr-TI/TI bilayer. So the bottom surface state electrons dominates in our Cr-TI single layer and the corresponding illustrations of current-induced longitudinal spin-orbit field and magnetization switching are given in Figure 3-3a-b. We should notice that based on our model, the switching direction of Cr-TI single layer may not be fixed, since from sample to sample, both top and bottom surface state electrons have chance to dominate the current-induced SOT and switching behavior depending on the growth method and the material details.

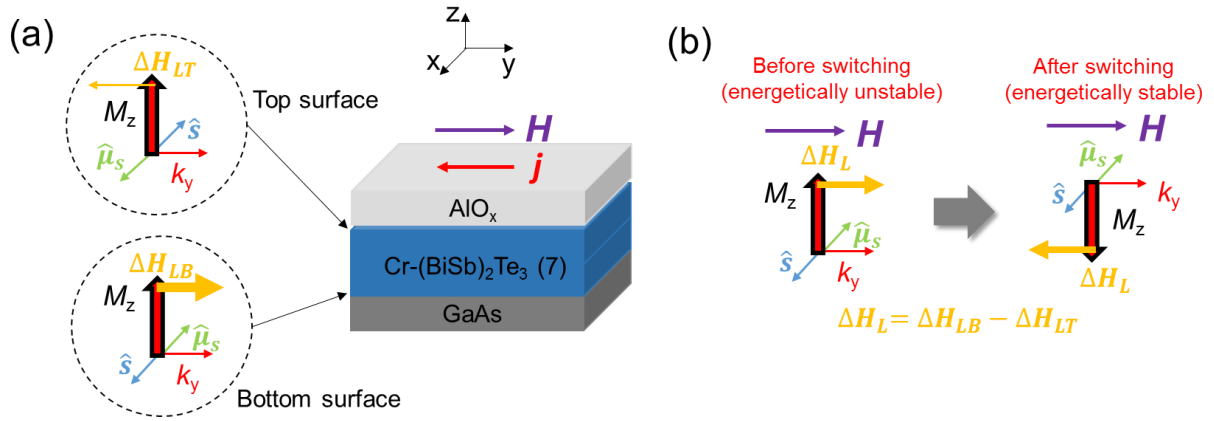


Figure 3-3 Model for topological surface state induced (longitudinal) damping-like spin-orbit field and magnetization switching in the Cr-TI single layer. (a) Longitudinal spin-orbit field generated by top and bottom surface state in the Cr-TI single layer with initial magnetization along +z direction. Both top and bottom surface give rise to spin-orbit field, but bottom surface gives larger spin-orbit field due to large Dirac electron density at bottom surface (bigger arrow indicates stronger spin-orbit field). (b) Total longitudinal spin-orbit field in the Cr-TI single layer is given by $\Delta H_L = \Delta H_{LB} - \Delta H_{LT}$. Since bottom surface dominates the total spin-orbit field, ΔH_L is still pointing along +y direction. This spin-orbit field leads magnetization switching in the presence of +y direction external magnetic field.

In this section, a basic SOT model is proposed without detailed theory behind, and this model can be used to explain the SOT phenomena in TI-based magnetic systems. Although we are not sure what the determining reason is for this giant SOT and the positive spin torque ratio now, it is still deserving verification of this model since more detailed theory could be potentially added into this simple model and make it comprehensive. The only detailed theory for TI-based SOT is introduced by Mark H Fischer et al. [36], but both magnitude and direction of SOT cannot be explained conclusively using their theory (other unknown factors, such as band topology, may

also give rise to this giant SOT). We will use this model to understand experiments done in the following two sections.

3.2 Magnetic doping position dependent study

In the Cr-(BiSb)₂Te₃/(BiSb)₂Te₃ bilayer, the magnetic dopant, Cr, is uniformly distributed at the bottom ~3 nm. Since the top surface state electrons are far away from the magnetic moments, the current-induced SOT and switching behavior are dominated by the bottom surface state electrons. This experiment makes use conceive following magnetic doping position dependent studies.

We grow three Cr-TI/TI heterostructures with different modulation doping positions for the Cr-TI layer. They are Cr-(BiSb)₂Te₃ (3)/(BiSb)₂Te₃ (9), (BiSb)₂Te₃ (9)/Cr-(BiSb)₂Te₃ (3) and (BiSb)₂Te₃ (3)/Cr-(BiSb)₂Te₃ (3)/ (BiSb)₂Te₃ (3) (see Figure 3-4), where the Cr-TI/TI represents that Cr-TI is at the bottom, and results of Cr-(BiSb)₂Te₃/(BiSb)₂Te₃ are already reported in section 2.2.2. Based on the model of surface state induced SOTs, Cr-TI/TI and TI/Cr-TI have opposite longitudinal spin-orbit fields. When the same current and external magnetic field are applied along +y direction, Cr-TI/TI prefers magnetization pointing up, whereas TI/Cr-TI prefers magnetization pointing down. This is due to the opposite chirality of top and bottom surface states as we discussed in section 3.1. For the TI/Cr-TI/TI trilayer, we expect that current-induced spin-orbit field is much smaller compared with Cr-TI/TI and TI/Cr-TI bilayer, since both top surface state electrons and bottom surface state electrons are quite far away from the magnetic moment (~3 nm). Based on first-principle calculation, the depth of topological surface state wavefunctions is around 3 nm [26]. Even assume that surface state electrons can penetrate 3 nm, the total spin-orbit field generated by current in this TI/Cr-TI/TI trilayer has to be small due to the vertical symmetry. The contributions from top and bottom surface state electrons cancel out each other.

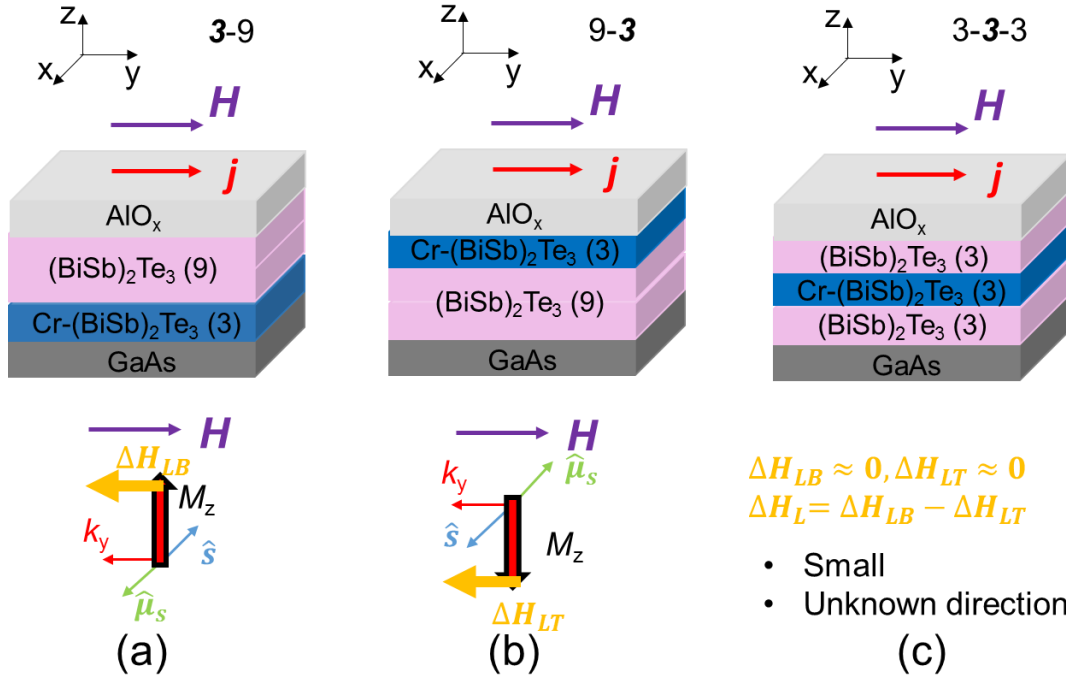


Figure 3-4 Magnetic doping position dependent longitudinal spin-orbit field. (a) When the Cr-TI is at the bottom, bottom surface state electrons give rise to a large longitudinal spin-orbit field along $M \times z \times j_b$ direction. The preferred direction is +z direction and final spin-orbit field is along $-y$ direction. Bold italic number represents the thickness of magnetic layer, and layer represented by the left number is below the layer represented by the right number. This rule applies for all the figures in this thesis. (b) When the Cr-TI is at the top, top surface state electrons give rise to a large longitudinal spin-orbit field along $-M \times z \times j_b$ direction. The preferred direction is -z direction and final spin-orbit field is along $-y$ direction. (c) When the Cr-TI is at the middle and both top and bottom surface states are separated from magnetic moments no less than 3nm, the current-induced spin-orbit field will be small since both top and bottom surface state electrons are quite far away from the magnetic moment. The direction of spin-orbit field depends on the relative strength of residual top and bottom spin-orbit fields.

We carry out the measurement of the SOT in these three samples. Results of **3-9** is shown in Figure 2-10 and results of **9-3** and **3-3-3** are shown in Figure 3-5, where the bold italic number represents the thickness of magnetic layer, and layer represented by the left number is below the layer represented by the right number (this rule applies throughout this thesis). Both **9-3** and **3-3-3** are n-type with well-defined out-of-plane magnetic hysteresis (ferromagnetism, see Figure 3-5a,c). Different from **3-9**, under external magnetic along +y direction, a positive current along +y direction gives rise to a positive second-harmonic resistance (a positive longitudinal spin-orbit field). This is consistent with the opposite configuration of **9-3** and **3-9**. We extract the spin-orbit field per A/cm^2 for both **9-3** and **3-9** and plot them in Figure 3-6. Their $\Delta H_L/J_C$ have opposite sign as we expect from the model of surface state induced SOTs.

In-plane second-harmonic resistance data of **9-3** and **3-3-3** have the same polarity, which indicates that current-induced longitudinal spin-orbit fields in them have the same direction (see Figure 3-5b,d). However, the magnitude of spin torque ratio in **3-3-3** is around one order smaller compared with that in **9-3** (see Figure 3-6). This is also consistent with the model of surface state induced SOTs, since surface state electrons are well separated from magnetic moments and vertical symmetry of film is maintained in **3-3-3**. However, we still observe nonzero spin-orbit field, which may result from the non-equal current density flowing through the top surface and bottom surface.

To understand the origin of this ‘small’ spin-orbit field (still very large compared with the heavy metal case), we further grow **10-3-10** sample. Again, we still observe finite positive $\Delta H_L/J_C$ in it (see Figure 3-6), and this indicates that even when the surface state electrons are truly far away from the magnetic moments (~ 10 nm), there is still small background spin-orbit field there.

At last, we grow two samples with **6-3-3** and **3-3-6** structure. Current-induced spin-orbit fields in them have the same direction. This result confirm that bulk SHE cannot be the origin of giant

SOTs again, since 6-**3-3** and 3-**3-6** have the opposite stack order from the point of bulk SHE mechanism.

In one word, except for the case when the magnetic moment is touching surface states, we observe fairly ‘small’ spin-orbit field with the same direction in 3-**3-3**, 10-**3-10**, 6-**3-3** and 3-**3-6**. This is what we expect from the model of surface state induced SOTs. However, the origin of this ‘small’ spin-orbit field cannot be explained using this model. This deserves further exploration.

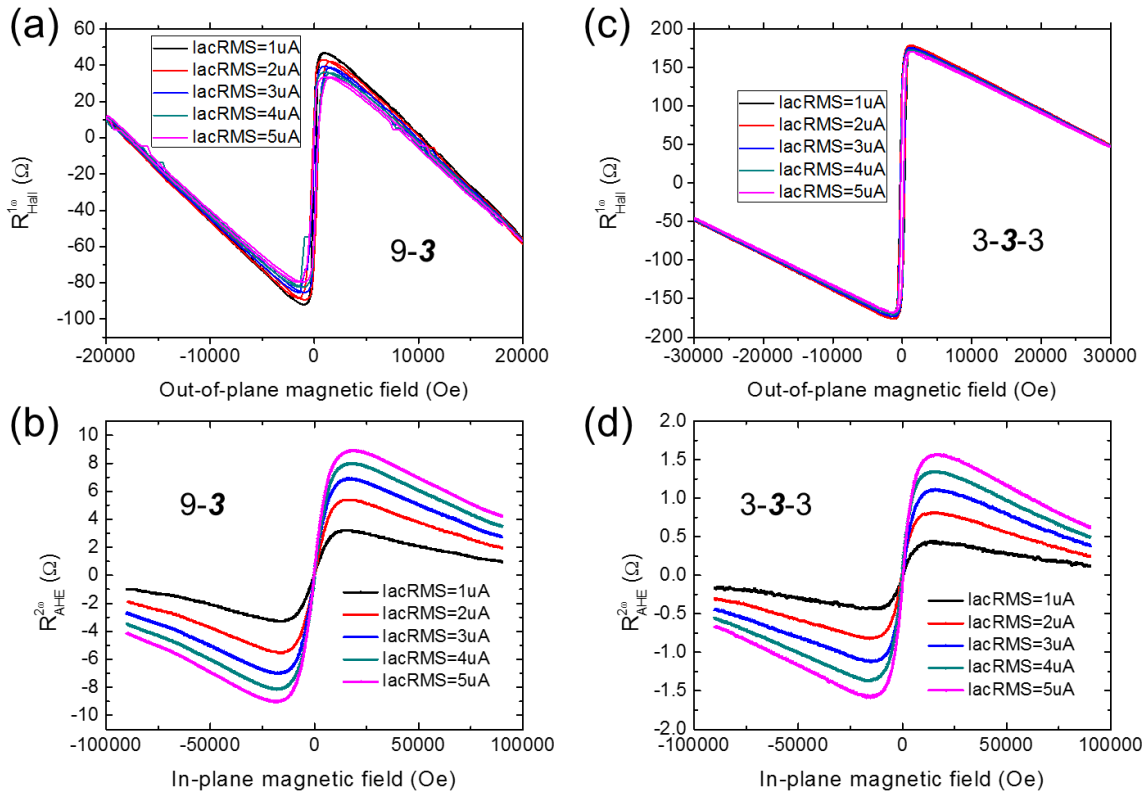


Figure 3-5 Out-of-plane magnetic hysteresis and in-plane second-harmonic resistance for the TI/Cr-TI bilayer (a-b) and the TI/Cr-TI/TI trilayer (c-d).

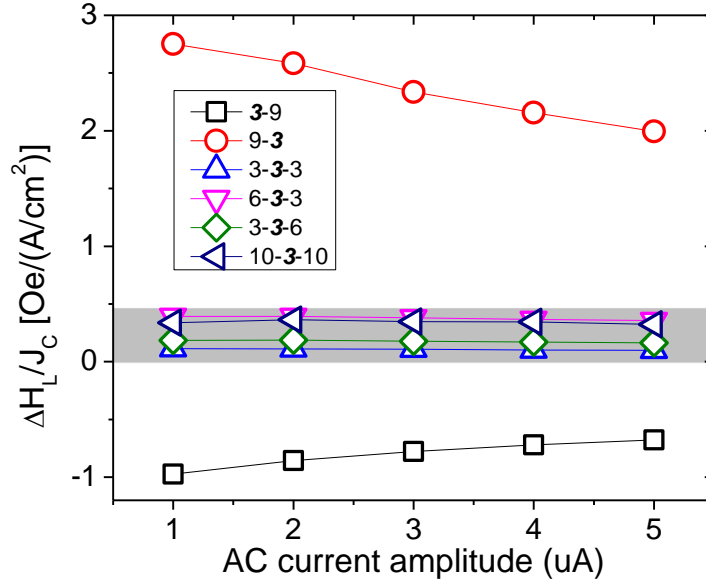


Figure 3-6 Current-induced longitudinal spin-orbit fields in different Cr-TI/TI heterostructures.

3.3 Electric-field controlled SOT

The Fermi level position of TI is very crucial for current-induced SOTs, if these SOTs are originated from surface state electrons. As we showed before in section 2.2.3, injection current could generate significant SOTs even in the uniformed Cr-doped TI single layer. The reason behind this is due to the different dielectric environment for top and bottom surface state, GaAs/Cr-TI and Cr-TI/ AlO_x . More specifically, the difference of Fermi level positions at top and bottom surface state bands results in different surface electron carrier densities. So, $\Delta H_L = \Delta H_{LB} - \Delta H_{LT} = M \times z \times (\vartheta_{BSS}j_b - \vartheta_{TSS}j_t)$ will still be significant if j_b and j_t have a large difference. Here, we assume that spin torque ratios for bottom (ϑ_{BSS}) and top (ϑ_{TSS}) surface are comparable, if not the same (due to different dielectric environments).

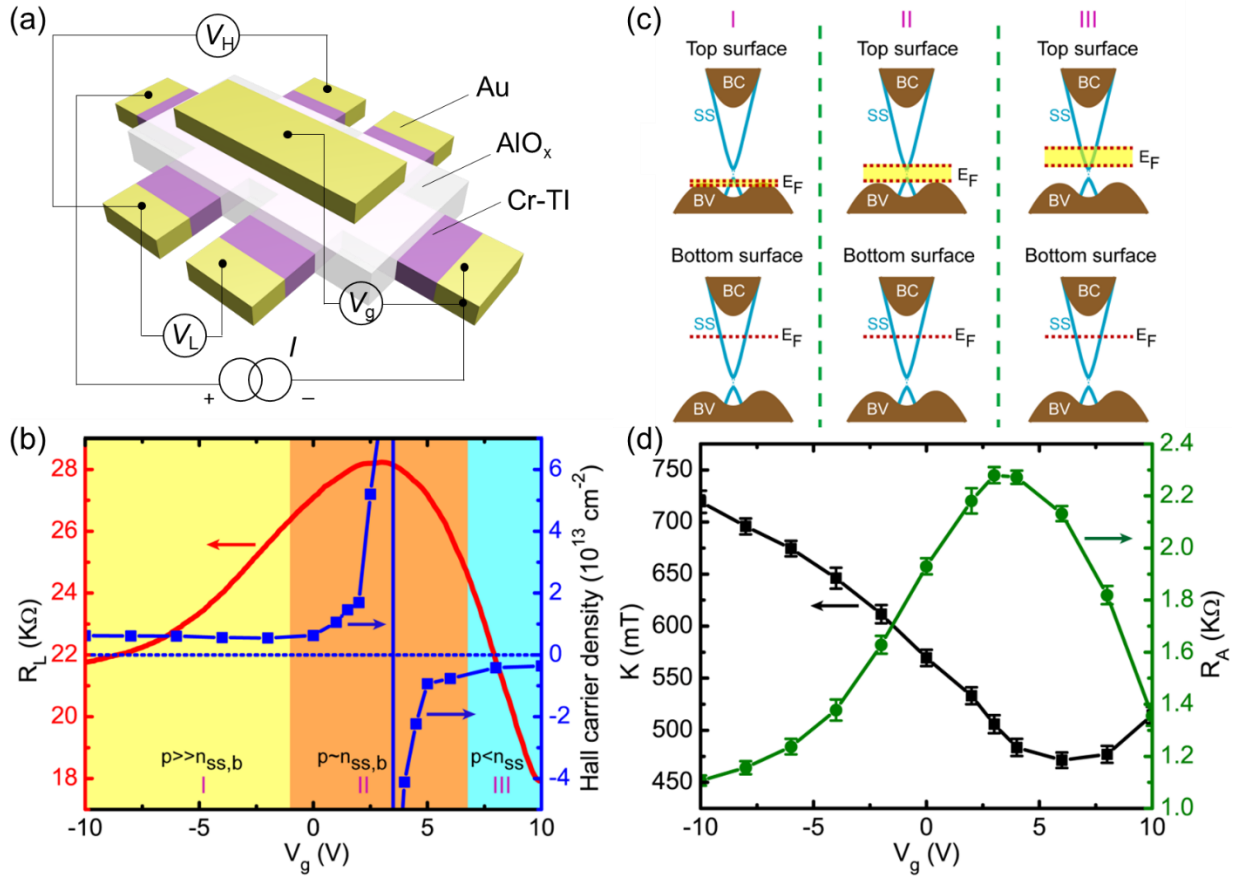


Figure 3-7 Electric-field effect on the sheet carrier density, top surface Fermi level, effective perpendicular anisotropy field and AHE coefficient in a Cr-TI single layer. (a) Schematic of the top-gated FET device. The AlO_x layer is around 20 nm, and the Cr-TI layer is around 7 nm. (b) Dependence of longitudinal resistance and Hall carrier density on the gate voltage. Colored area I, II and III show the different gate voltage regions. (c) Fermi level at top and bottom surface state in regime I, II and III shown in (b). (d) Dependence of anisotropy field and R_A on the gate voltage. (b), (c) and (d) are provided by Yabin Fan *et al.*

In this section, we use top gate to tune the Fermi level of top surface for a Cr-TI single layer, and study the electric field effect on current-induced SOTs. The schematics of the top-gated FET device and relevant measurement setup are shown in Figure 3-7a. The ambipolar electrical

transport is observed in this Cr-TI single layer (see Figure 3-7b), which indicates the Fermi level of top surface state can be continuously tuned across the Dirac surface state band gap. Typically, when TIs are doped with magnetic dopants, a surface state band gap will open due to the loss of π berry phase [42]. In addition, for the high-dielectric Cr-(BiSb)₂Te₃, penetration depth of electric field is around 3 nm considering the metallic nature of surface state electrons. Therefore, only Fermi level of the top surface state can be tuned through the gate voltage. The ambipolar transport of this Cr-TI single layer can be described by dividing it into three regimes (corresponding Fermi level positions are show in Figure 3-7c): I, top Fermi level is buried in the bulk valence band, and bottom Fermi level is pinned in the surface conduction band. Therefore, top bulk hole density is much larger than the bottom Dirac electron density (top Dirac hole density is very small). II, top Fermi level is around the Dirac surface band gap, and bottom Fermi level is in the surface conduction band. Therefore, top carrier density is much smaller than the bottom Dirac electron density. III, both top and bottom Fermi levels are in the surface conduction band, and top Fermi level is lower than the bottom. Therefore, top Dirac electron density is smaller compared with the bottom Dirac electron density. The reason for us to conclude that bottom Fermi level is pinned at surface conduction band is from the Shubinkov-de Haas (SdH) quantum oscillation study of a reference undoped sample (BiSb)₂Te₃ [43]. Note that in Cr-doped (BiSb)₂Te₃, the mobility is too low to observe the SdH quantum oscillation. However, since Cr is only around 8%, the overall band structure of Cr-(BiSb)₂Te₃ should be similar with (BiSb)₂Te₃. To extract the current-induced (in-plane) longitudinal spin-orbit field using Eq. 18, dependences of perpendicular anisotropy coefficient K and R_A are plotted in Figure 3-7d.

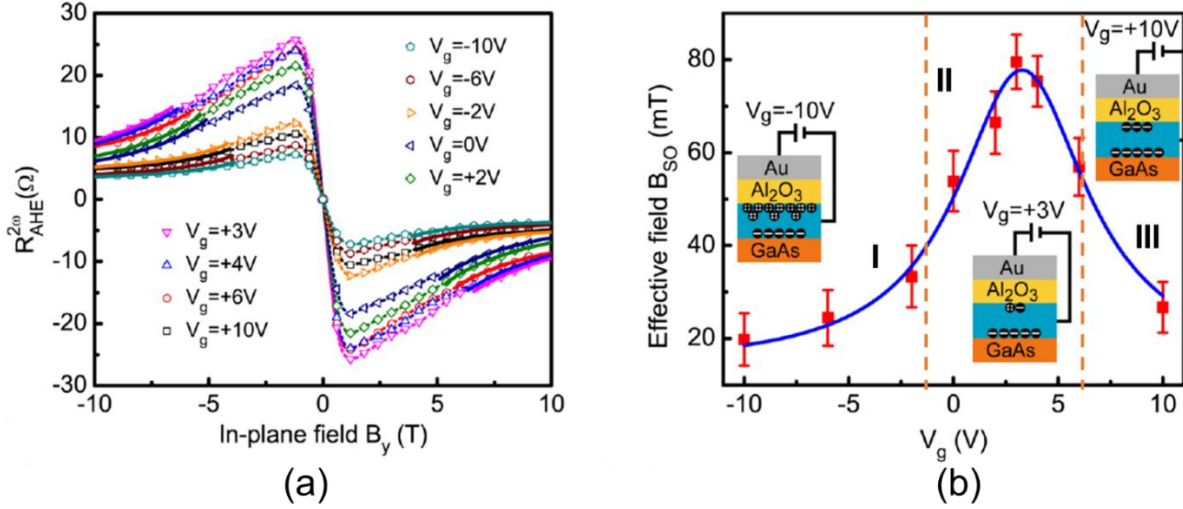


Figure 3-8 Electric-field effect on the in-plane second-harmonic resistance and current-induced longitudinal spin-orbit field in the Cr-TI single layer. Inset illustrations in (b) represent the carrier distribution in the Cr-TI single layer under a sepecific gate votlage. (a) and (b) are provide by provided by Yabin Fan *et al.*.

The dependence of in-plane second-harmonic resistance on the gate voltage for the Cr-TI single layer is shown in Figure 3-8a. Clear modulation is observed, which indicates that gate voltage has a significant effect on the magnitude of current-induced spin-orbit field. Figure 3-8b shows the extracted values of current-induced spin-orbit field under different gate voltage. The dependence of spin torque ratio (assume that the saturation magnetization remains constant for this sample under different gate voltages) is somehow correlated with the carrier distribution shown in Figure 3-7b. In regime II, only bottom surface state electrons contribute to the total spin-orbit field. But in regime I and III, top Dirac holes and top Dirac electrons cancel part of the contribution from the bottom surface state electrons, resulting a relatively smaller spin-orbit field. Here, we should notice that Dirac hole and Dirac electron generate SOTs with the same direction, since under the electric field, both carrier momentum and spin chirality are opposite (spin is locked to momentum

in an anticlockwise fashion for Dirac holes from top view). The magnitude of the SOT can be tuned by a factor of four using gate voltage, which is much larger than the heavy metal case, thanks to the semiconducting nature of TIs [44].

In one word, we show that electric-field can control the SOT in TI-based magnetic systems significantly, which may contribute the future low power nonvolatile electronics, if we could combine the gate control and nonvolatile nature of ferromagnetism.

Chapter 4. Summary and outlook

In this thesis, we reviewed the history of spintronics and introduced the spin torque based switching mechanism for both current-based and voltage-based MRAMs. For STT-MRAMs, the switching current is relatively high and we introduced SOT-MRAM with potentially lower switching current. The critical parameter in determining the critical current is the spin torque ratio, and we showed that in TIs, the spin torque ratio can be three orders of magnitude larger than heavy metals. In addition, we used magnetic doping position dependent study to show that surface state with spin-momentum locking is probably the source for this giant SOT. Combined with gate control, the magnitude of SOT can be changed by a factor of four, and it may help realize the future reconfigurable instant-on nonvolatile electronics.

However, there are still two critical issues for the real application of TIs in spintronics:

1. Demonstration of the giant SOT at room temperature is still lacking.
2. High mobility of metallic surface states is required for current going through the surface channel.

For the first issue, we plan to grow TI/FM heterostructures and study the SOT in them, where FM is ferromagnetic at room temperature. For the second issue, we need to further increase the TI film quality to recover their intrinsic properties [45].

References

- [1] "International Technology Roadmap of Semiconductor (ITRS)," 2013.
- [2] G. Binasch, P. Grünberg, F. Saurenbach, and W. Zinn, "Enhanced magnetoresistance in layered magnetic structures with antiferromagnetic interlayer exchange," *Physical Review B*, vol. 39, no. 7, pp. 4828-4830, 1989.
- [3] M. N. Baibich, J. M. Broto, A. Fert, F. N. Van Dau, F. Petroff, P. Etienne, G. Creuzet, A. Friederich, and J. Chazelas, "Giant Magnetoresistance of (001)Fe/(001)Cr Magnetic Superlattices," *Physical Review Letters*, vol. 61, no. 21, pp. 2472-2475, 1988.
- [4] J. G. Alzate, "Voltage-Controlled Magnetic Dynamics in Nanoscale Magnetic Tunnel Junctions," Electrical Engineering, University of California, Los Angeles, 2014.
- [5] J. C. Slonczewski, "Current-driven excitation of magnetic multilayers," *Journal of Magnetism and Magnetic Materials*, vol. 159, no. 1-2, pp. L1-L7, 1996.
- [6] L. Berger, "Emission of spin waves by a magnetic multilayer traversed by a current," *Physical Review B*, vol. 54, no. 13, pp. 9353-9358, 1996.
- [7] J. Sun, "Spin-current interaction with a monodomain magnetic body: A model study," *Physical Review B*, vol. 62, no. 1, pp. 570-578, 2000.
- [8] P. Khalili Amiri, Z. M. Zeng, J. Langer, H. Zhao, G. Rowlands, Y. J. Chen, I. N. Krivorotov, J. P. Wang, H. W. Jiang, J. A. Katine, Y. Huai, K. Galatsis, and K. L. Wang, "Switching current reduction using perpendicular anisotropy in CoFeB–MgO magnetic tunnel junctions," *Applied Physics Letters*, vol. 98, no. 11, pp. 112507, 2011.
- [9] S. Ikeda, K. Miura, H. Yamamoto, K. Mizunuma, H. D. Gan, M. Endo, S. Kanai, J. Hayakawa, F. Matsukura, and H. Ohno, "A perpendicular-anisotropy CoFeB–MgO magnetic tunnel junction," *Nat Mater*, vol. 9, no. 9, pp. 721-4, Sep, 2010.
- [10] K. C. Chun, H. Zhao, J. D. Harms, T. H. Kim, J. P. Wang, and C. H. Kim, "A Scaling Roadmap and Performance Evaluation of In-Plane and Perpendicular MTJ Based STT-MRAMs for High-Density Cache Memory," *IEEE Journal of Solid-State Circuits*, vol. 48, no. 2, pp. 598-610, Feb, 2013.
- [11] T. Maruyama, Y. Shiota, T. Nozaki, K. Ohta, N. Toda, M. Mizuguchi, A. A. Tulapurkar, T. Shinjo, M. Shiraishi, S. Mizukami, Y. Ando, and Y. Suzuki, "Large voltage-induced magnetic anisotropy change in a few atomic layers of iron," *Nat Nanotechnol*, vol. 4, no. 3, pp. 158-61, Mar, 2009.
- [12] S. E. Barnes, J. Ieda, and S. Maekawa, "Rashba spin-orbit anisotropy and the electric field control of magnetism," *Sci Rep*, vol. 4, pp. 4105, 2014.
- [13] N. Nagaosa, J. Sinova, S. Onoda, A. H. MacDonald, and N. P. Ong, "Anomalous Hall effect," *Reviews of Modern Physics*, vol. 82, no. 2, pp. 1539-1592, 2010.
- [14] K. Garello, I. M. Miron, C. O. Avci, F. Freimuth, Y. Mokrousov, S. Blugel, S. Auffret, O. Boulle, G. Gaudin, and P. Gambardella, "Symmetry and magnitude of spin-orbit torques in ferromagnetic heterostructures," *Nat Nanotechnol*, vol. 8, no. 8, pp. 587-93, Aug, 2013.

- [15] L. Ejsing, M. F. Hansen, A. K. Menon, H. A. Ferreira, D. L. Graham, and P. P. Freitas, "Planar Hall effect sensor for magnetic micro- and nanobead detection," *Applied Physics Letters*, vol. 84, no. 23, pp. 4729, 2004.
- [16] A. Chernyshov, M. Overby, X. Liu, J. K. Furdyna, Y. Lyanda-Geller, and L. P. Rokhinson, "Evidence for reversible control of magnetization in a ferromagnetic material by means of spin-orbit magnetic field," *Nature Physics*, vol. 5, no. 9, pp. 656-659, 2009.
- [17] I. M. Miron, K. Garello, G. Gaudin, P. J. Zermatten, M. V. Costache, S. Auffret, S. Bandiera, B. Rodmacq, A. Schuhl, and P. Gambardella, "Perpendicular switching of a single ferromagnetic layer induced by in-plane current injection," *Nature*, vol. 476, no. 7359, pp. 189-93, Aug 11, 2011.
- [18] I. M. Miron, G. Gaudin, S. Auffret, B. Rodmacq, A. Schuhl, S. Pizzini, J. Vogel, and P. Gambardella, "Current-driven spin torque induced by the Rashba effect in a ferromagnetic metal layer," *Nat Mater*, vol. 9, no. 3, pp. 230-4, Mar, 2010.
- [19] G. Yu, P. Upadhyaya, Y. Fan, J. G. Alzate, W. Jiang, K. L. Wong, S. Takei, S. A. Bender, L. T. Chang, Y. Jiang, M. Lang, J. Tang, Y. Wang, Y. Tserkovnyak, P. K. Amiri, and K. L. Wang, "Switching of perpendicular magnetization by spin-orbit torques in the absence of external magnetic fields," *Nat Nanotechnol*, vol. 9, no. 7, pp. 548-54, Jul, 2014.
- [20] L. Liu, C. F. Pai, Y. Li, H. W. Tseng, D. C. Ralph, and R. A. Buhrman, "Spin-torque switching with the giant spin Hall effect of tantalum," *Science*, vol. 336, no. 6081, pp. 555-8, May 4, 2012.
- [21] L. Liu, O. J. Lee, T. J. Gudmundsen, D. C. Ralph, and R. A. Buhrman, "Current-Induced Switching of Perpendicularly Magnetized Magnetic Layers Using Spin Torque from the Spin Hall Effect," *Physical Review Letters*, vol. 109, no. 9, 2012.
- [22] X. Qiu, K. Narayanapillai, Y. Wu, P. Deorani, D. H. Yang, W. S. Noh, J. H. Park, K. J. Lee, H. W. Lee, and H. Yang, "Spin-orbit-torque engineering via oxygen manipulation," *Nat Nanotechnol*, vol. 10, no. 4, pp. 333-8, May, 2015.
- [23] K. L. Wang, J. G. Alzate, and P. K. Amiri, "Low-power non-volatile spintronic memory: STT-RAM and beyond," *Journal of Physics D-Applied Physics*, vol. 46, no. 7, pp. 074003, Feb 20, 2013.
- [24] J. Kim, J. Sinha, M. Hayashi, M. Yamanouchi, S. Fukami, T. Suzuki, S. Mitani, and H. Ohno, "Layer thickness dependence of the current-induced effective field vector in Ta|CoFeB|MgO," *Nat Mater*, vol. 12, no. 3, pp. 240-5, Mar, 2013.
- [25] S. Emori, U. Bauer, S. M. Ahn, E. Martinez, and G. S. Beach, "Current-driven dynamics of chiral ferromagnetic domain walls," *Nat Mater*, vol. 12, no. 7, pp. 611-6, Jul, 2013.
- [26] H. Zhang, C.-X. Liu, X.-L. Qi, X. Dai, Z. Fang, and S.-C. Zhang, "Topological insulators in Bi₂Se₃, Bi₂Te₃ and Sb₂Te₃ with a single Dirac cone on the surface," *Nature Physics*, vol. 5, no. 6, pp. 438-442, 2009.
- [27] M. Konig, S. Wiedmann, C. Brune, A. Roth, H. Buhmann, L. W. Molenkamp, X. L. Qi, and S. C. Zhang, "Quantum spin hall insulator state in HgTe quantum wells," *Science*, vol. 318, no. 5851, pp. 766-70, Nov 2, 2007.

- [28] B. A. Bernevig, T. L. Hughes, and S. C. Zhang, "Quantum spin Hall effect and topological phase transition in HgTe quantum wells," *Science*, vol. 314, no. 5806, pp. 1757-61, Dec 15, 2006.
- [29] M. Z. Hasan, and C. L. Kane, "Colloquium: Topological insulators," *Reviews of Modern Physics*, vol. 82, no. 4, pp. 3045-3067, 2010.
- [30] X.-L. Qi, and S.-C. Zhang, "Topological insulators and superconductors," *Reviews of Modern Physics*, vol. 83, no. 4, pp. 1057-1110, 2011.
- [31] Y. L. Chen, J. G. Analytis, J. H. Chu, Z. K. Liu, S. K. Mo, X. L. Qi, H. J. Zhang, D. H. Lu, X. Dai, Z. Fang, S. C. Zhang, I. R. Fisher, Z. Hussain, and Z. X. Shen, "Experimental realization of a three-dimensional topological insulator, Bi₂Te₃," *Science*, vol. 325, no. 5937, pp. 178-81, Jul 10, 2009.
- [32] J. Tang, L. T. Chang, X. Kou, K. Murata, E. S. Choi, M. Lang, Y. Fan, Y. Jiang, M. Montazeri, W. Jiang, Y. Wang, L. He, and K. L. Wang, "Electrical Detection of Spin-Polarized Surface States Conduction in (Bi_{0.53}Sb_{0.47})₂Te₃ Topological Insulator," *Nano Lett*, vol. 14, no. 9, pp. 5423-9, Sep 10, 2014.
- [33] D. Kong, Y. Chen, J. J. Cha, Q. Zhang, J. G. Analytis, K. Lai, Z. Liu, S. S. Hong, K. J. Koski, S. K. Mo, Z. Hussain, I. R. Fisher, Z. X. Shen, and Y. Cui, "Ambipolar field effect in the ternary topological insulator (Bi_xSb_{1-x})₂Te₃ by composition tuning," *Nat Nanotechnol*, vol. 6, no. 11, pp. 705-9, Nov, 2011.
- [34] C. H. Li, O. M. van 't Erve, J. T. Robinson, Y. Liu, L. Li, and B. T. Jonker, "Electrical detection of charge-current-induced spin polarization due to spin-momentum locking in Bi₂Se₃," *Nat Nanotechnol*, vol. 9, no. 3, pp. 218-24, Mar, 2014.
- [35] André Dankert, Johannes Geurs, M. Venkata Kamalakar, and S. P. Dash, "Room Temperature Electrical Detection of Spin Polarized Currents in Topological Insulators," <http://arxiv.org/abs/1410.8038>, 2014.
- [36] Mark H Fischer, Abolhassan Vaezi, Aurelien Manchon, and E.-A. Kim, "Large Spin Torque in Topological Insulator/Ferromagnetic Metal Bilayers," <http://arxiv.org/abs/1305.1328>, 2013.
- [37] Y. Fan, P. Upadhyaya, X. Kou, M. Lang, S. Takei, Z. Wang, J. Tang, L. He, L. T. Chang, M. Montazeri, G. Yu, W. Jiang, T. Nie, R. N. Schwartz, Y. Tserkovnyak, and K. L. Wang, "Magnetization switching through giant spin-orbit torque in a magnetically doped topological insulator heterostructure," *Nat Mater*, vol. 13, no. 7, pp. 699-704, Jul, 2014.
- [38] Z. H. Zhu, G. Levy, B. Ludbrook, C. N. Veenstra, J. A. Rosen, R. Comin, D. Wong, P. Dosanjh, A. Ubaldini, P. Syers, N. P. Butch, J. Paglione, I. S. Elfimov, and A. Damascelli, "Rashba Spin-Splitting Control at the Surface of the Topological Insulator Bi₂Se₃," *Physical Review Letters*, vol. 107, no. 18, 2011.
- [39] P. D. C. King, R. C. Hatch, M. Bianchi, R. Ovsyannikov, C. Lupulescu, G. Landolt, B. Slomski, J. H. Dil, D. Guan, J. L. Mi, E. D. L. Rienks, J. Fink, A. Lindblad, S. Svensson, S. Bao, G. Balakrishnan, B. B. Iversen, J. Osterwalder, W. Eberhardt, F. Baumberger, and P. Hofmann, "Large Tunable

- Rashba Spin Splitting of a Two-Dimensional Electron Gas in Bi_2Se_3 ,” *Physical Review Letters*, vol. 107, no. 9, 2011.
- [40] A. R. Mellnik, J. S. Lee, A. Richardella, J. L. Grab, P. J. Mintun, M. H. Fischer, A. Vaezi, A. Manchon, E. A. Kim, N. Samarth, and D. C. Ralph, “Spin-transfer torque generated by a topological insulator,” *Nature*, vol. 511, no. 7510, pp. 449-51, Jul 24, 2014.
- [41] M. S. Bahramy, P. D. King, A. de la Torre, J. Chang, M. Shi, L. Patthey, G. Balakrishnan, P. Hofmann, R. Arita, N. Nagaosa, and F. Baumberger, “Emergent quantum confinement at topological insulator surfaces,” *Nat Commun*, vol. 3, pp. 1159, 2012.
- [42] H.-Z. Lu, J. Shi, and S.-Q. Shen, “Competition between Weak Localization and Antilocalization in Topological Surface States,” *Physical Review Letters*, vol. 107, no. 7, 2011.
- [43] L. He, X. Kou, M. Lang, E. S. Choi, Y. Jiang, T. Nie, W. Jiang, Y. Fan, Y. Wang, F. Xiu, and K. L. Wang, “Evidence of the two surface states of $(\text{Bi}_{0.53}\text{Sb}_{0.47})_2\text{Te}_3$ films grown by van der Waals epitaxy,” *Sci Rep*, vol. 3, pp. 3406, 2013.
- [44] R. H. Liu, W. L. Lim, and S. Urazhdin, “Control of current-induced spin-orbit effects in a ferromagnetic heterostructure by electric field,” *Physical Review B*, vol. 89, no. 22, 2014.
- [45] Y. Xu, I. Miotkowski, C. Liu, J. Tian, H. Nam, N. Alidoust, J. Hu, C.-K. Shih, M. Z. Hasan, and Y. P. Chen, “Observation of topological surface state quantum Hall effect in an intrinsic three-dimensional topological insulator,” *Nature Physics*, vol. 10, no. 12, pp. 956-963, 2014.